CHALMERS
UNIVERSITY OF TECHNOLOGY

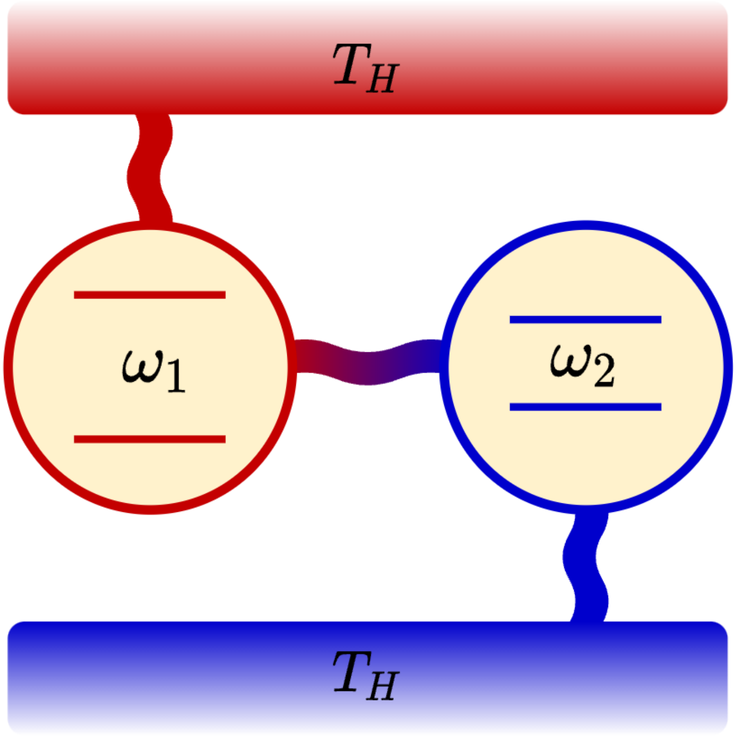

Quantum thermal machine driven by electrical noise

A study in quantum thermodynamics using superconducting qubits

Master's thesis in Physics

Simon Sundelin

Department of Microtechnology and Nanoscience (MC2)

CHALMERS UNIVERSITY OF TECHNOLOGY
Gothenburg, Sweden 2022
www.chalmers.se

MASTER'S THESIS 2022

Quantum thermal machine driven by electrical noise

A study in quantum thermodynamics using superconducting qubits

Simon Sundelin

CHALMERS
UNIVERSITY OF TECHNOLOGY

Department of Microtechnology and Nanoscience (MC2)
Wallenberg Centre for Quantum Technology
202Q-lab
CHALMERS UNIVERSITY OF TECHNOLOGY
Gothenburg, Sweden 2022

Quantum thermal machine driven by electrical noise
A study in quantum thermodynamics using superconducting qubits
Simon Sundelin

Supervisor: Aamir Ali, Quantum Technology Laboratory, Chalmers
Examiner: Simone Gasparinetti, Quantum Technology Laboratory, Chalmers

Master's Thesis 2022
Department of Microtechnology and Nanoscience (MC2)
Quantum Technology Laboratory (QT)
202Q-Lab
Chalmers University of Technology
SE-412 96 Gothenburg
Telephone +46 31 772 1000

Cover: Depiction of a quantum thermal machine where two artificial atoms acts as the working medium allowing heat to flow between a cold and hot reservoir.

Printed by Chalmers Reproservice
Gothenburg, Sweden 2022

Quantum thermal machine driven by electrical noise
A study in quantum thermodynamics using superconducting qubits
Simon Sundelin
Department of Microtechnology and Nanoscience (MC2)
Chalmers University of Technology

Abstract

Akin to the quantum advantage a quantum computer has over its classical counterpart, the possibility of such an advantage existing in thermodynamics has in recent years gained more attention. A paradigmatic goal within the field of quantum thermodynamics, is the realization of quantum thermal machines which is the topic of this thesis. We present a novel quantum thermal machine consisting of two strongly coupled flux tuneable qubits and two microwave waveguides acting as thermal baths which predominantly couples to separate transitions of the hybridized qubits. The quantum thermal machine is then driven by controlling the dephasing rate of the qubits using white noise and synthesized thermal fields inside of the heat baths. We also present a theoretical model of the expected heat flows between these heat baths. Using independently extracted parameters, this model coincides with the experimentally observed heat currents measured to be on the order of a single aW. The results demonstrate the workings of a heat valve and helps to pave the way for further studies in the search of a quantum advantage in thermodynamics.

Keywords: Quantum thermodynamics, Heat valve, Heat flow, Quantum thermal machine, Circuit QED

Acknowledgements

I would like to thank and give my gratitude to my examiner Simone Gasparinetti for giving me the wonderful opportunity to work on this very interesting project while providing the necessary support and knowledge. I also give a heartfelt thanks to my supervisor Aamir Ali whom I have worked with on this project and who made the many hours spent in the lab both fun and an invaluable learning experience. Additionally I want to show my gratitude to Claudia Castillo Moreno and Mikael Kervinen who fabricated the device used in this thesis. I do also give my deepest thanks to all members of the 202Q-Lab who all made this past half year very fun and full of new experiences. Finally I would like to thank all my friends and family for the support I have received throughout my master project.

Simon Sundelin, Gothenburg, 12-2021

Contents

1

Introduction

Since the advent of quantum mechanics, pioneered by physicist such as Werner Heisenberg, Niels Bhor and others in the early decades of the 20th century, many fields of research has been revamped as a consequence. This quantum revolution allowed for, among others, an explanation of the periodic table and enabled the development of many new technologies such as the laser and transistor, upon which our modern society is based upon [1]. However, in the year of 2012, Serge Haroche and David Wienland received a Nobel price for their work in accessing single quantum systems [2,3]. This pioneering work laid the foundation for the second quantum revolution allowing for measuring and control capabilities on single quantum systems [4].

In light of this second revolution, the suggestion that R.P Feynman made in the early '80s suddenly became feasible. His suggestion was that a *quantum computer* which is a computer harnessing the quantum mechanical properties of superposition and entanglement, might be able to solve certain problems exponentially faster then its classical counterpart [5, 6]. The interest to build such a quantum computer is therefore high but in order to achieve a *quantum advantage* in computing many challenges must first be overcome. These include the construction of high fidelity and error tolerant quantum processors along with useful algorithms to solve problems which would require polynomial time when simulated on a classical computer. In 2019 such a quantum advantage was demonstrated by Arute et al. at Google [7]. They performed a quantum mechanical algorithm on their quantum processor in 200 seconds, whereas the classical equivalent algorithm when performed on a state-of the art classical supercomputer was estimated to take approximately 10000 years. However, according to IBM an optimized algorithm would on their classical supercomputer only take 2,5 days [8]. While this is not as great an improvement between the quantum processor and its classical counterpart as Google claimed, these results still highlights the advantage that the quantum computer holds over the classical computer for this particular algorithm.

The main building blocks in the quantum processor utilized by Arute et al. are so called *superconducting qubits* which are artificial atoms engineered with superconducting electrical circuits. In essence, these are LC-circuits operating in the microwave regime but with the inductor exchanged by a *Josephson junction* (JJ) resulting in a non-linearity in the circuits potential energies. This anharmonicity in the qubits energy levels results in that the energy spectrum of this artificial atom then resembles that of an actual atom [9]. The details of the working principles behind the superconducting qubit will be described in greater detail in section 2.1, but the most important consequence of this anharmonicity is that the qubit can be treated as a two-level system (TLS). This allows one to selectively excite the qubit to only the first excited state since the energy difference between the ground and first excited state corresponding to $\hbar\omega_{01}$ is not equal to that between the first and second excited state $\hbar\omega_{12}$. The most simple type of superconducting qubit is the Single Cooper-pair Box (SCPB) consisting of a superconducting island onto which so-called Cooper-pairs (see section 1.1) can tunnel to and from. However, these type of qubits are very sensitive to charge fluctuations resulting in fluctuating energy levels, making it very hard to control. A better alternative to the SCPB is instead the *transmon* qubit where an additional capacitance has been added to shunt the superconductors, resulting in stable energy levels. Additionally, instead of using only a single JJ, one can construct a transmon consisting of a superconducting quantum interference device (SQUID) which allows one to tune the energy levels of the qubit by applying an external magnetic field [10]. Such a flux-tuneable transmon is one of the main building blocks in the device that is studied in this thesis.

Not only are superconducting qubits a good basis upon which quantum processors can be built, but they are also useful to explore quantum optics which is the study of light-matter interactions [11]. The study of such interactions on a superconducting circuitry platform is referred to as circuit quantum electrodynamics (cQED). However, the interaction between photons and e.g. an artificial atom is limited by the fine structure constant and results in a rather weak coupling between them. In cQED it is however possible to engineer both the atom and the environment in order to reach the strong or even ultra-strong coupling regime where information losses to the environment no longer exceed the coupling strength between the photons and atom [26]. One way of reducing losses to the environment is to restrict the environment to one dimension using waveguides [13]. In cQED such a one-dimensional waveguide consists of a coplanar transmission line which directs the fields/photons inside of it. A waveguide can therefore be used as a channel through which one can probe or control e.g. a qubit.

At this point we have given a short introduction to the two main building-blocks used in this thesis, that is the concept of a waveguide and a flux-tuneable transmon. However, the topic of this thesis lies in the realm of *quantum thermodynamics*, that is the fusion of quantum mechanics and thermodynamics. Akin to the quantum advantage found in computing the field of quantum thermodynamics tries to answer the question if the utilization of quantum mechanics in thermodynamics could yield a similar advantage [14]. Furthermore, the motivation behind exploring the impact that quantum mechanics could have on thermodynamics also lies in that the miniaturization of electronics require us to understand the thermodynamical properties of quantum systems. In the search of quantum features within thermodynamics, a lot of theoretical work has been done [52–56], but a robust experimental platform upon which quantum thermodynamical experiments can be performed is still needed. Apart from e.g. metallic-islands [58] and nitrogen-vacancy centers [59], a promising candidate for such a platform is cQED. On this platform, current state of the art experiments as performed by Yong Lu et.al. [57] involves the measurement of

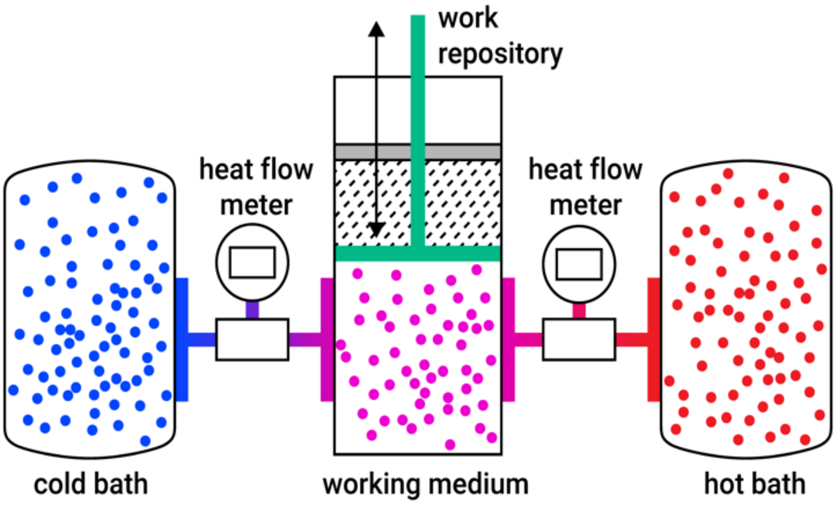

Figure 1.1: Illustration of a thermal machine consisting of a hot and cold heat baths with a working medium in between. The heat flow can be measured between the baths and the working medium from which work can be extracted. Credit: Daniel Špaček / Neuron collective.

heat flows on the aW scale from a ”hot” environment (being heated with a resistive element) into a ”cold” waveguide. The heat flows, corresponding to the transfer of photons, was in those experiments enabled by a single superconducting qubit acting as the transfer mechanism.

A paradigmatic goal in the field of quantum thermodynamics is the the realization of quantum thermal machines, which like their classical counterpart (see Figure 1.1) can utilize work to refrigerate (refrigerator) or transform heat to useful work (heat engine) [15]. In a heat engine the heat flows with the temperature gradient between a hot and a cold thermal bath while in the case of a refrigerator the heat flows against the temperature gradient. In addition to the impact which quantum refrigerators and engines could have on emerging technologies, the study of heat flows in the quantum realm could deepen our understanding in how energy flows on the nanoscale [16].

In this thesis we present a novel quantum thermal machine driven by electrical noise in a cQED platform. We demonstrate the theoretical model along with the experimentally measured heat flows when operating the device as a heat valve. The device itself consists of two strongly coupled flux tuneable qubits coupled to two waveguides acting as heat baths, the temperature of which are controlled by synthesized thermal fields. In essence, because of the coupling scheme and the strong coupling between the qubits, the two waveguides only couple to two individual qubits with different transition frequencies. By then applying synthesized environmental noise we show that excitation transfer takes place, enabling measurable heat to flows between the waveguides. The scope of the project was limited to experimental measurements and theoretical modeling. The design and fabrication of the device has therefore largely been omitted in this thesis but can for a similar device be found in the thesis by Kowshik [47]. Before elaborating further on the principles behind our quantum thermal machine we first need to discuss the main physical phenomenon allowing for the creation of superconducting artificial atoms.

1.1 Superconductivity

In the year of 1911, H.K. Onnes [21] first discovered the ground breaking phenomenon known as *superconductivity* when he observed that the electrical resistance of mercury vanished bellow a certain critical temperature T_c. Ensuing this discovery, the property of superconductivity was then found in several other metals with different critical temperatures. The reason of why we observe this lack of electrical resistance bellow certain temperatures is discussed by R.P Feynman in his lectures on physics [22]. The interactions between electrons and vibrations of the atoms in the lattice (phonons) bring about a small effective attraction between the electrons. Therefore, it is energetically more favorable for two electrons to form a so called *Cooper-pair* rather than remaining separated. The remarkable consequence of this is that the two electrons, which independently are spin 1/2 fermions, instead turn into a spin zero boson when forming such a pair. Also, in contrast to Fermi particles, these Cooper-pairs are Bose particles meaning that there is no limit to how many such particles can occupy any particular state. The pairing of electrons then opens up a gap in their previously continuous spectrum of allowed energy states [23]. This results in that possible excitations must have some minimum energy and that excitations involving small energies such as the scattering of electrons, becomes impossible. This is what give rise to superconductivity. Unfortunately, the attraction is very weak resulting in that the electrons are easily separated and Cooper-pairs break up under only small thermal agitations. The thermal energy needed to break a Cooper-pair is in turn dependent on the critical temperature of the material. At sufficiently low temperatures however, a large fraction of the electrons will occupy their lowest energy state and the following pair formation gives rise to a Bose-Einstein condensate. Since a Cooper-pair can be considered a Bose particle, it is then possible to write the real-space wave equation of this composite boson as

$$\psi(\mathbf{r}) = \sqrt{\rho(\mathbf{r})}\mathbf{e}^{\mathbf{i}\varphi(\mathbf{r})} \tag{1.1}$$

where we have a spatial dependence of the pair density ρ and phase φ.

The advent of superconductors opened up many new fields of research and applications. In particular, the process of Cooper-pairs tunneling through a thin insulator separating two superconductors, forming the aforementioned Josephson junction, is of great importance. This element is what allows for the creation of nearly dissipationless, non-linear circuit elements and is the foundation upon which the superconducting qubit lies upon.

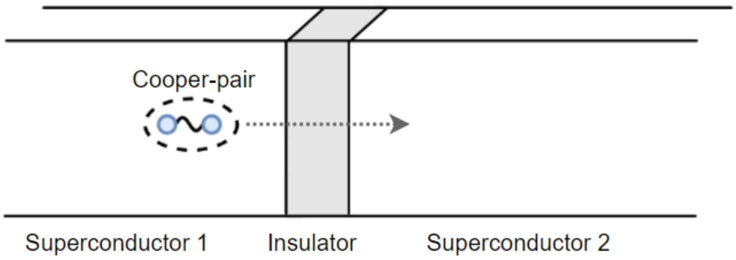

Figure 1.2: Illustration of a Josephson junction. The Cooper-pair tunnels across the insulator which acts as a potential barrier before continuing into the next superconductor.

1.2 The quantum thermal machine

In essence, our quantum thermal machine presented in section 3.1.1 consists of two waveguides acting as thermal baths, each coupled to a qubit. The photons inside of the waveguides are bosons which do not obey the Pauli exclusion principle. The average number of thermal photons n_B with a frequency ω inside of a waveguide/bath is thus characterized by the Bose-Einstein distribution when in thermal equilibrium and obeys [17]

$$n_B = \frac{1}{e^{\frac{\hbar\omega}{k_B T}} - 1} \tag{1.2}$$

where T is the temperature of the bath and k_B Boltzmann constant. Therefore the number of photons in the waveguide is dictated by the temperature of the heat bath. Contrary to the thermal baths, the number of excitations in a qubit (e.g. an atom) when in a thermal equilibrium with a heat bath obeys the Fermi-Dirac distribution

$$n_i = \frac{1}{e^{\frac{\hbar\omega_i}{k_B T}} + 1}. \tag{1.3}$$

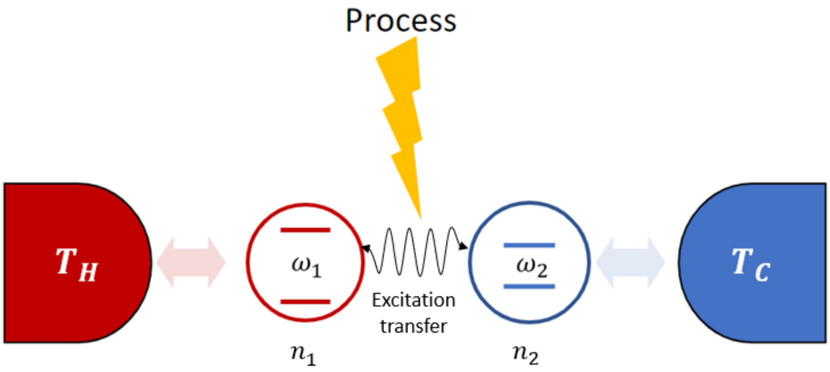

Figure 1.3: Depiction of the working principles behind the quantum thermal machine used in this thesis. There are two qubits, each coupled to a waveguide acting as a thermal bath. Through the means of process not yet specified, excitation transfer can take place.

This entails that the population (number of excitations) of a qubit depend on the temperature of the thermal bath to which it is coupled and will stabilize around some certain value at thermal equilibrium. Because the population also is dependent on the transition frequency of the qubit, the number of excitations will differ even if $T_H = T_C$, that is even if the hot bath has the same temperature as the cold bath. If one then introduces some process as illustrated in Figure 1.3, that results in a transfer of excitations between the two qubits and thus new populations e.g. $n_1' = n_2'$, the subsequent equilibration with the thermal bath will result in a net heat flow. In order to conceptually illustrate this heat flow we study the example when the qubit coupled to the hot heat bath has a transition frequency $\omega_1 > \omega_2$ and the process results in the new populations $n_1' = n_2'$ as illustrated in Figure 1.4. If the initial populations satisfied $n_1 > n_2$, the qubit coupled to the hot heat bath need to absorb photons in order to equalize back while the other qubit emits photons, back into the cold bath. This increase of photons in the cold bath and decrease of photons in the hot bath thus entail a net heat flow with the temperature gradient and this particular initial condition for the populations therefore correspond to a heat engine. If the initial populations instead satisfy $n_1 < n_2$, the equalization process will instead result in that the qubit coupled to the cold heat bath will absorb photons while the other emits photons. In this instance, the net heat flow goes against the temperature gradient and this setup therefore correspond to a refrigerator. Note that in both the case of a heat engine and a refrigerator, the work performed goes into the respective waveguides.

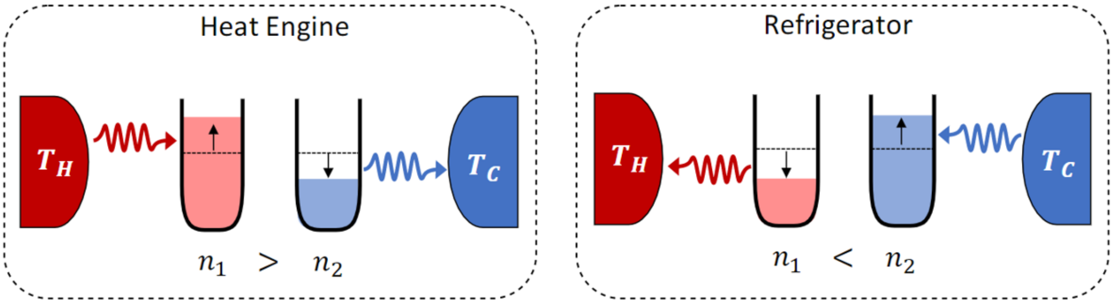

Figure 1.4: The working principles of the quantum thermal machine. When the initial populations satisfy $n_1 > n_2$, the system behaves as a heat engine due to the thermalization with the heat baths. Photons will either be emitted or absorbed by the qubits in order to equalize back to their initial populations.With the initial populations instead satisfying $n_1 < n_2$, the system acts as a refrigerator because photons will in this case flow from the cold to the hot heat bath.

1.3 Environment-assisted quantum transport

In this thesis the process resulting in a transfer of populations as mentioned in the previous section is performed using environment assisted quantum transport induced by pure dephasing noise. To illustrate this transfer we consider the simple example given by Rebentrost et al. [18] where they discuss noise assisted transport for a two-site system (comparable to our two qubits in the thermal machine). This two-site system that consists of site $|1\rangle$ and $|2\rangle$ can each host one excitation has the Hamiltonian

$$\mathcal{H} = \frac{\Delta}{2}(|1\rangle\langle 1| - |2\rangle\langle 2|) + \frac{g}{2}(|1\rangle\langle 2| + |2\rangle\langle 1|) \tag{1.4}$$

where the coupling strength between the two sites is denoted g and the energy mismatch is denoted by Δ. If initially there is an excitation at site 1 the system will evolve coherently in the absence of any noise. When looking at this system on the Bloch sphere it can be viewed as a state precessing about the z-axis at an angle $\theta = \sin^{-1}\left(\frac{g}{\Omega}\right)$ where the well known Larmor frequency is defined as $\Omega = \sqrt{\Delta^2 + g^2}$. In the case of the excitation initially located at site 1, one finds that the average probability of finding the excitation at site 2 is $\sin^2(\theta)$. However, in the case of the energy mismatch between the two sites is sufficiently large, that is if $\Delta >> g$, no transfer will occur and the excitation will remain at site 1. This regime with very weak or no noise is thus often refereed to as the quantum localization-regime [19]. More specifically the system is in a pure state where the excitation, initially localized at site 1 evolves into a superposition of energy eigenstates but with a vanishing probability of being found at the other site.

The introduction of noise into the environment will however have an effect on the transport capabilities of the system. In the case of such a noisy environment, the two sites are characterized by a Lindblad master equation which depend on the pure dephasing rate γ_ϕ (as discussed in section 2.4.2). Assuming that this dephasing rate is equal for both sites, the system obeys the Bloch equations [20]. Using conventional Bloch analysis one finds that the system, instead of remaining localized at site 1 as in the case without any noise, diffuses over both sites and ultimately ends up in a uniform mixture of $|1\rangle$ and $|2\rangle$. In this fully mixed state the excitation has a 50% chance of being found at either of the two sites. This process of diffusion, that is the effect of the pure dephasing, can be treated as a random walk on the Bloch sphere with steps of of length θ occurring at the rate of γ_ϕ.

In summary, the addition of white noise to a system with an excitation initially localized at site 1 induces dephasing resulting in that we go from a pure state to a mixed state;

$$\text{pure state of } |1\rangle \longrightarrow \text{mixed state of } |1\rangle \text{ and } |2\rangle.$$

Since we have gone from the quantum localized regime to a mixed state where the other site can be reached, this process is termed environment-assisted quantum transport. Thus by controlling the pure dephasing rate using white noise, the system can be put into a state where $n_1' = n_2'$. If these two sites consists of the qubits as described in the previous section, this system (including the waveguides) has the potential to operate as a quantum thermal machine.

2

Theory

In this chapter we give a more rigorous treatment of the elements and theory upon which the content of this thesis is based. We begin by building a quantized theoretical model of the qubit and the waveguide which are our two main components. Later and following an explanation of how these components interact with each other, we discuss the effects of the light-matter interactions taking place between the electromagnetic field present inside of the waveguide and the qubit. Finally we then turn to an analysis of the noise induced heat flow to be expected from our measurements.

2.1 Quantization of superconducting circuits

This project revolves around superconducting artificial atoms coupled to microwave waveguides which can be viewed as one dimensional transmission lines. In essence, a superconducting artificial atom is a harmonic oscillator in the form of a LC-circuit but with non-linear energy levels. Therefore we begin this section by describing the quantization of a LC-circuit to which the Josephson junction will be introduced, allowing us to model the superconducting artificial atom i.e. the qubit. We then proceed by introducing the quantization of the field inside of a semi-infinite waveguide before describing how this field interacts with the qubit in the next section.

2.1.1 The quantized LC oscillator

Following Devoret (1997) [24], the quantization of the LC-circuit begins by defining the node flux ϕ as a generalized coordinate of the system depicted in Figure 2.1. This node flux is defined as the time integral of the voltage V over the capacitor

$$\phi(t) = \int_0^t V(\tau) d\tau \tag{2.1}$$

meaning that $V(t) = \dot{\phi}$ which allow us to express the energy contributions from the two non-dissipative elements in the system in terms of this new coordinate. The kinetic energy stored in the capacitance is

$$\mathcal{T} = \frac{1}{2} C \dot{\phi}^2 \tag{2.2}$$

and the potential energy stored in the inductor is

$$\mathcal{V} = \frac{1}{2L} \phi^2. \tag{2.3}$$

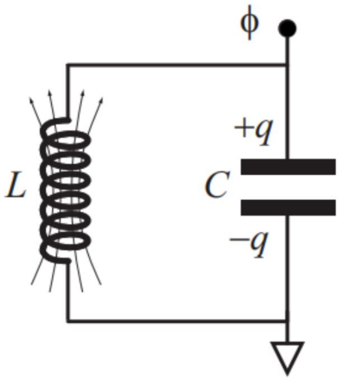

Figure 2.1: Illustration of the LC circuit with inductance L and capacitance C. The node flux ϕ is defined as the time integral of the voltage V across the capacitor. Furthermore, q represents the node (capacitor) charge.

The resulting Lagrangian for the system is therefore given by

$$\mathcal{L}(\phi, \dot{\phi}, t) = \frac{1}{2}C\dot{\phi}^2 - \frac{1}{2L}\phi^2. \tag{2.4}$$

In order to write and later quantize the Hamiltonian $\mathcal{H}$, we need the conjugate momentum of the flux which is defined as

$$p = \frac{\delta \mathcal{L}}{\delta \dot{\phi}} = C\dot{\phi} \tag{2.5}$$

which corresponds to the node charge given by

$$p = \int_{-\infty}^{t} I(\tau)\mathrm{d}\tau \tag{2.6}$$

where I is the current at the node. The Hamiltonian is now obtained through a Legendre transformation [12] of the Lagrangian, resulting in

$$\mathcal{H}\left(\phi, p, t\right) = p\dot{\phi} - \mathcal{L}\left(\phi, \dot{\phi}, t\right) = \frac{p^2}{2C} + \frac{\phi^2}{2L}. \tag{2.7}$$

At this point it is worth to note the resemblance this Hamiltonian has to that of a harmonic oscillator $\mathcal{H} = \frac{p^2}{2m} + \frac{m}{2}\omega^2 x^2$. This comparison enables us to identify the resonance frequency $\omega = 1/\sqrt{LC}$ and mass $m = C$ of the LC-oscillator. Following the standard quantization procedure we now promote the coordinates to operators as

$$\begin{aligned} \phi &\rightarrow \hat{\phi} \\ p &\rightarrow \hat{p} \end{aligned} \tag{2.8}$$

with the commutation relation

$$[\hat{\phi}, \hat{p}] = i\hbar. \tag{2.9}$$

Furthermore, by introducing the ladder operators $a^\dagger$ and a defined as

$$\hat{\phi} = \sqrt{\frac{\hbar}{2}\frac{1}{C\omega}}\left(a^\dagger + a\right) \tag{2.10}$$

$$\hat{p} = i\sqrt{\frac{\hbar}{2}C\omega}\left(a^\dagger - a\right), \tag{2.11}$$

the Hamiltonian can be rewritten as

$$\mathcal{H} = \hbar\omega\left(a^\dagger a + \frac{1}{2}\right) \tag{2.12}$$

which we again note is the familiar expression for a quantum harmonic oscillator with evenly spaced linear energy levels.

The ladder operators $a^\dagger$ and a follows the bosonic commutation relation $\left[a, a^\dagger\right] = 1$ and when operating on an energy eigenstate $|n\rangle$ they fulfill

$$a^\dagger|n\rangle = \sqrt{n+1}|n+1\rangle \tag{2.13}$$

$$a|n\rangle = \sqrt{n}|n-1\rangle. \tag{2.14}$$

and the number operator $a^\dagger a = N$ obeys the eigenequation

$$N|n\rangle = n|n\rangle \tag{2.15}$$

Thus they can be viewed as creation and annihilation operators which creates or annihilates one quanta $\hbar\omega$ of energy in the system. The apparent problem of infinite negative energy, obtained by applying the annihilation operator repeatedly on some energy eigenstate, is resolved thanks to the ladder operators obeying the bosonic commutation relation. This entails that

$$n = \langle n|N|n\rangle = \left\langle n \left| a^\dagger a \right| n \right\rangle = (a|n\rangle)^\dagger a|n\rangle \geqslant 0$$

meaning that the smallest eigen-value is 0 and thus $a|0\rangle = 0$.

2.1.2 The artificial atom

In order to introduce non-linearity into the harmonic energy spectrum found in the quantized LC circuit we turn to the nonlinear element that is the JJ, as presented in section 1.1. The behaviour of such a junction was predicted by David Josephson [25] in the year of 1962, and is governed by two important equations. The current arising from the phase difference $\varphi(t)$ of the cooper pairs tunneling across the junction can be expressed as

$$I(t) = I_c \sin\varphi(t) \tag{2.16}$$

where I_c is the so called critical current of the junction and depends on the temperature and material. The voltage across the junction do also depend on the phase difference between the superconductors and is expressed as

$$V(t) = \frac{2e}{\hbar}\frac{\partial\varphi(t)}{\partial t}. \tag{2.17}$$

It then becomes evident that this phase difference corresponds to the time integral of the voltage over the JJ [26] which we know is the magnetic flux

$$\varphi(t) = \frac{2e}{\hbar}\int_0^t V\left(t'\right)dt' = 2\pi\frac{\Phi}{\Phi_0}, \tag{2.18}$$

where we have defined the magnetic flux quantum $\Phi_0 = \frac{h}{2e}$. Using these expressions in the relationship between voltage and current over an inductor $V = L\dot{I}$, one finds that the JJ acts like a non-linear inductor

$$L_J = \frac{2\pi}{\Phi_0 I_c \cos\varphi} = \frac{\Phi_0}{2\pi I_c}\frac{1}{\cos\left(2\pi\Phi/\Phi_0\right)}. \tag{2.19}$$

So in contrast to a normal inductor we note that L_J depends on the flux. Similarly to how one can calculate the energy stored in an inductor, the energy stored in the JJ can then be expressed as

$$E = \int dtVI = -E_J \cos\left(\frac{2\pi}{\Phi_0}\Phi\right) \tag{2.20}$$

where the Josephson energy $E_J = \frac{\phi_0 I_c}{2\pi}$ is the maximum energy that can be stored in the junction. Therefore, by replacing the linear inductor of our LC oscillator by a JJ as illustrated in Figure 2.2 b), the circuit is rendered nonlinear. Such a circuit with an added shunting capacitance, is what in textbooks is refereed to a transmon and is what is most often used for a superconducting anharmonic oscillator. In this thesis we are however considering a slightly more complex system where instead of one JJ we have two JJ connected in parallel and thus forming the aforementioned SQUID, see Figure 2.2 c). This element behaves like a single JJ but with the difference that its critical current $I_c \to 2I_c\left|\cos\left(\pi\frac{\Phi}{\Phi_0}\right)\right|$ can be tuned by a magnetic flux Φ threading the SQUID [9] which results in a flux dependence of the Josephson energy $E_J(\Phi)$.

If one does not include the shunting capacitance C_S and connect the circuit to a voltage source V via a gate capacitance C_G, we instead have a circuit corresponding to a single cooper pair box (SCPB) with a Hamiltonian

$$\mathcal{H} = \frac{Q^2}{2C_\Sigma} - E_J(\Phi)\cos\varphi. \tag{2.21}$$

Here $C_\Sigma = C_G + 2C_J$ also includes the small capacitance C_J of the junction. In essence we now have a superconducting island inhabited by $n = \frac{Q}{2e}$ cooper pairs. By tuning the voltage V, one can then effectively change the number of cooper pairs on the island resulting in the new charge $Q = (2e\left(n - n_g\right))$ where we have a offset charge given by $n_g = \frac{C_G V}{2e}$. By promoting the number of cooper pairs and the phase difference to operators we can quantize our circuit and write the Hamiltonian as

$$\mathcal{H} = 4E_C\left(\hat{N} - n_g\right)^2 - E_J(\Phi)\cos\hat{\varphi} \tag{2.22}$$

where we have introduced the so called charging energy $E_C = \frac{e^2}{2C_\Sigma}$. However, this Hamiltonian do not have an exact solution but thanks to the commutation relation between our operators, $[\hat{\varphi}, \hat{n}] = i$, the Hamiltonian can be rewritten in the phase basis as

$$\mathcal{H} = E_C\left(-i\frac{\partial}{\partial\hat{\varphi}} - n_g\right)^2 - E_J(\Phi)\cos\hat{\varphi}. \tag{2.23}$$

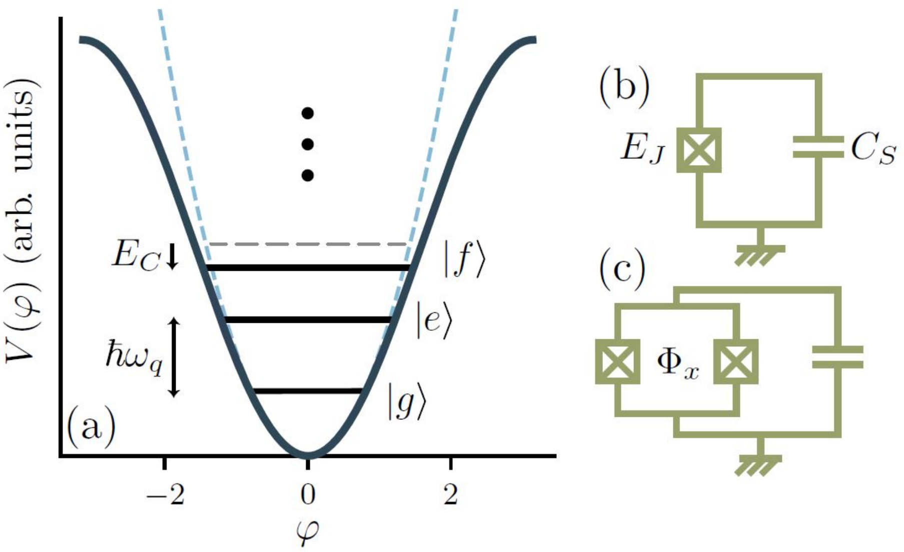

Figure 2.2: (a) The quadratic potential well with linear energy levels (dashed lines) of the LC oscillator, each with an energy difference of $\hbar\omega_q$. The filled line indicates the cosine potential well for the transmon with anharmonic energy levels characterized by the anharmonicity $\alpha \approx -E_C$. (b) The transmon is a SCPB with the addition of the shunt capacitor C_S and with the cross indicating the Josephson junction with Junction capacitance C_J and Josephson energy E_J. (c) Exchanging the single JJ for a SQUID the transmon becomes flux tuneable by means of applying an external flux Φ_x. Figure taken from [26].

Using Mathieu's functions [28] this Hamiltonian yields the exact energy levels which depend on $\frac{E_J}{E_C}$, Φ and n_g. However, when fixing the values for the flux and energy ratio, which for a SCPB often is $\frac{E_J}{E_C} \approx 1$ [29], the energy levels are strongly anharmonic but prone to noise in the n_g variable as seen in Figure 2.3, which can strongly influence the decoherence of the qubit. As mentioned previously, the transmon does in contrast to the SCPB include a shunting capacitor C_S which increases C_Σ thus decreasing E_C which in turn increases $\frac{E_J}{E_C}$. The result of this is that the anharmonicity becomes smaller but the qubit becomes much less prone to noise and the coherence time of the transmon when $\frac{E_J}{E_C} >> 1$ is therefore greatly improved compared to the SCPB [9].

Similar to the Hamiltonian in equation 2.22 but with a modified E_C, the energy eigenvalues when approximated in the $\frac{E_J}{E_C} >> 1$ limit as can be obtained as

$$E_n \approx -E_J(\Phi) + \sqrt{8E_C E_J(\Phi)}\left(n + \frac{1}{2}\right) - \frac{E_C}{12}\left(6n^2 + 6n + 3\right). \tag{2.24}$$

In this limit we have a weakly anharmonic oscillator with transition energies given by

$$\hbar\omega_{eg}(\Phi) = (E_1 - E_0) \approx \sqrt{8E_C E_J\left|\cos\left(\pi\frac{\Phi}{\Phi_0}\right)\right|} - E_C \tag{2.25}$$

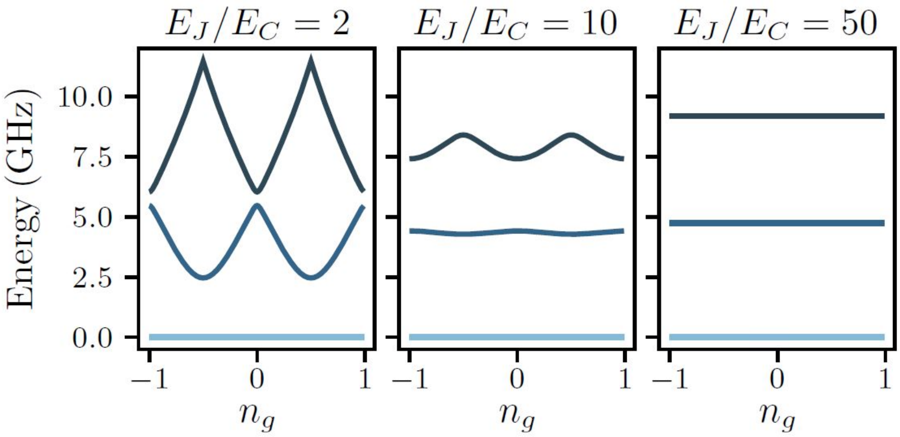

Figure 2.3: The energy difference of the first three energy levels for different rations of E_J/E_C. Note that when increasing this ration the system becomes less sensitive to noise in the offset charge variable n_g. However the anharmonicity decreases meaning that one has to be mindful of the interplay between letting the device having large anharmonicity versus being noise sensitive. Figure taken from [26].

as illustrated in Figure 2.2 a). The absolute anharmonicity between the first $|e\rangle$ and second excited state $|f\rangle$ is for this system $\alpha \approx -E_C$ and when only operating the transmon in the subspace of the ground and first excited state it can be regarded as a TLS with the Hamiltonian

$$\mathcal{H} = \frac{\hbar\omega_{eg}(\Phi)}{2}\sigma_z \tag{2.26}$$

where the Pauli z matrix is defined as $\sigma_z = |g\rangle\langle g| - |e\rangle\langle e|$.

In summary we now have a model for the qubits used in this thesis whose transition frequencies can be tuned by applying an external flux as per equation 2.25. Furthermore, by operating the qubit as a TLS it can be described by the Hamiltonian given in equation 2.26. However, as of this point we do not have any tools to interact with the qubit. By utilizing coplanar waveguides one can both detect photons scattered by the system as well sending in signals to directly control the qubit. In addition to this, it is also of interest how the photons inside of the waveguide interacts with the qubit, which relates to the detected photon flux in and out of the waveguide when operating the device as a quantum thermal machine.

2.1.3 Coplanar waveguide

The primary structure in cQED used to interact with transmons are transmission lines which are one dimensional coplanar waveguides (CPW) which are the two-dimensional equivalent to a coaxial cable. In addition to acting as a channel through which one can transmit and read signals they are in thesis used as quantum optical reservoirs that constitutes the heat baths for the quantum thermal machine. We initially start with the model of a open ended waveguide before restricting it to the case of the semi-infinite waveguide used in this thesis by choosing appropriate boundary conditions.

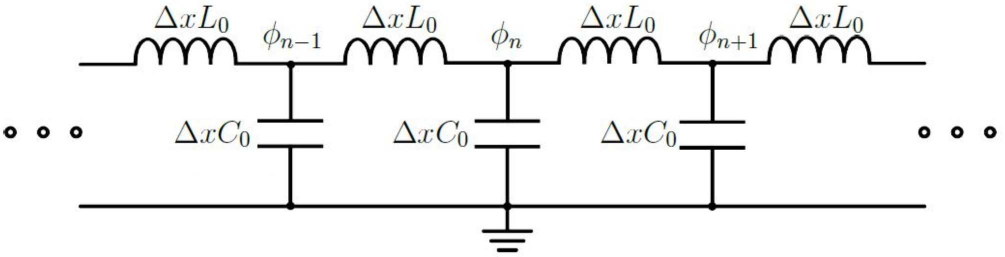

Figure 2.4: Distributed element representation of the transmission line. It consists of a a large number of inductors in series and parallelly connected grounded capacitors with inductance L_0 and capacitance C_0 per unit length Δx respectively. Figure taken from [12].

As illustrated in Figure 2.4, the transmission line can be modeled using distributed elements [30, 31]. With this representation the system of length d can be seen as an infinite chain of LC-oscillators with a capacitance C_0 and inductance L_0 per unit length spaced evenly with the interval Δx and flux nodes at ϕ_n. Because we already know how to quantize a LC-circuit we start by formulating the Lagrangian in the continuous limit where we consider $N \longrightarrow \infty$ segments of the transmission line of length $\Delta x \longrightarrow 0$. The Langrangian can thus be expressed as the integral

$$\mathcal{L} = \int_0^d \left[\frac{C_0}{2} \left(\frac{\partial \phi(x,t)}{\partial t} \right)^2 + \frac{1}{2L_0} \left(\frac{\partial \phi(x,t)}{\partial x} \right)^2 \right] \mathrm{d}x \tag{2.27}$$

where $\phi(x,t)$ now corresponds to the flux density at point x and time t. The equation of motion can now be derived from the Euler-Lagrange equation of motion

$$\frac{\partial}{\partial t} \frac{\partial \mathcal{L}}{\partial \frac{\partial \phi}{\partial (t,x)}} - \frac{\partial \mathcal{L}}{\partial \phi} = 0 \tag{2.28}$$

from which one obtains

$$\frac{\partial \phi^2(x,t)}{\partial t^2} - v^2 \frac{\partial \phi^2(x,t)}{\partial x^2} = 0. \tag{2.29}$$

This we note have the same form as the wave equation with the speed of light inside of the waveguide $v = \frac{1}{\sqrt{L_0 C_0}}$ being determined by the capacitance and inductance per unit length. The wave equation has the well known general solution of the form

$$\phi(x,t) = \sum_{n=1}^{\infty} A_n \cos(k_n x + \alpha_n) \cos(k_n v t + \beta_n) \tag{2.30}$$

where the parameters A_n, k_n, α_n and β_n depends upon which boundary condition we choose for our transmission line. Both A_n and β_n are determined by the initial conditions but by defining open boundaries at the points $x = d$ and $x = 0$, the only way for equation 2.30 to be a solution to the wave equation is to have $\alpha_n = 0$ and $k_n = \frac{n\pi}{d}$. When substituting this solution into equation 2.27 we get

$$\mathcal{L} = \sum_{n=1}^{\infty} \frac{C_n}{2} \dot{\phi}_n^2 - \frac{\phi_n^2}{2L_n} \tag{2.31}$$

with $\phi_n = A_n \cos\left(k_n vt + \beta_n\right), C_n = \frac{C_0 d}{2}$ and $L_n = \frac{2L_0 d}{n^2\pi^2}$. As expected we note that this is simply an infinite chain of LC oscillators which we know how to quantize. The Hamiltonian can therefore be written as

$$\mathcal{H} = \sum_{n=1}^{\infty} \hbar\omega_n \left(a_n^\dagger a_n + \frac{1}{2}\right) \tag{2.32}$$

with the possible mode frequencies defined as $\omega_n = \frac{1}{\sqrt{L_N C_N}} = \frac{n\pi}{d}\frac{1}{\sqrt{L_0 C_0}}$. The previously mentioned regime that we are interested in for this thesis is the semi-infinite waveguide where the length d of the waveguide is very large. In this regime the frequency differences between the modes are extremely small meaning that essentially all modes are supported within the waveguide. The Hamiltonian for the semi-infinite waveguide therefore takes the the form of an infinite integral

$$\mathcal{H} = \int_0^{\infty} \hbar\omega \left(a_n^\dagger a_n + \frac{1}{2}\right) d\omega \tag{2.33}$$

where the annihilation and creation operators for the modes inside of the waveguide has been redefined to include that $d \longrightarrow \infty$. [32].

With this we now have quantized models for both the elements used in this thesis but as of yet we do not have the tools to describe their interactions with each other. Therefore, the next section elaborates on the interactions taking place between these elements.

2.2 Combined systems

This thesis lies within the realm of quantum thermodynamics and is studied on a cQED platform where our qubits interacts with the electromagnetic field inside of the waveguides. In order to describe this interaction we turn to some standard methods used in quantum optics, or more specifically the quantum optical master equation. This equation is needed in order to describe the dynamics of open systems such as a qubit coupled to the field inside of a waveguide. In addition to this we also present the Hamiltonians describing the interaction between the elements and the two new modes referred to as the symmetric and antisymmetric mode arising from having two qubits coupled to each other.

2.2.1 Open quantum systems

For a closed quantum system with few degrees of freedom the dynamics obeys the Schrödinger equation

$$i\hbar\frac{\mathrm{d}}{\mathrm{d}t}|\Psi\rangle = \mathcal{H}|\Psi\rangle \tag{2.34}$$

where the state vector $|\Psi\rangle$ evolves under the system Hamiltonian [34]. However, for many quantum mechanical systems it is often the case that that a single state vector is insufficient since it could be in a statistical mixture of states. Therefore the more general representation of the system which includes both pure and mixed states utilizes the density matrix defined as $\rho \equiv \sum_i p_i \left|\Psi_i\right\rangle \left\langle\Psi_i\right|$ where we have a probability p_i to be in the state $\left|\Psi_i\right\rangle$. By starting from the Shrödinger equation, the equation of motion governing the density matrix can be derived as [35]

$$\dot{\rho} = -i[\mathcal{H}, \rho]. \tag{2.35}$$

This equation is called the Von Neumann or Liouville equation and similarly to the Shrödinger equation, holds true for a closed or isolated system which entails that one has to account for enough degrees of freedom in order to use them. Unfortunately, in the case of a small system coupled to a larger system like a waveguide acting as a reservoir, the number of degrees of freedom is vast. However, most often the dynamics of interest are only related to a specific part of the combined system such as a qubit and we don't care about the rest. This reduction makes the subsystem of interest appear open and is termed an *open quantum system* and is done by tracing out the unwanted degrees of freedom of the environment from the Liouville equation. This leads to the so called *master equation* governing the evolution of an open quantum system, the derivation of which is covered extensively in literature [12, 35, 36]. In this thesis we are interested in the master equation governing an emitter such as a qubit coupled to the modes of the electromagnetic field in its environment and is expressed as [12]

$$\dot{\rho} = -i\left[\mathcal{H}, \rho\right] + \Gamma(n+1)\mathcal{D}\left[\sigma_-\right]\rho + \Gamma n\mathcal{D}\left[\sigma_+\right]\rho + \frac{\Gamma_\phi}{2}\mathcal{D}\left[\sigma_z\right]\rho. \tag{2.36}$$

Here the first term is the now familiar Liouvillian, evolving the system under its own Hamiltonian. This is then followed by *dissipators*, responsible for the dissipation in the master equation. Before elaborating on the terms constituting the dissipation we note that for a thermal bath in equilibrium, the average number of photons n at temperature T follows the Bose-Einstein distribution [37] given by equation 1.2. From this we see that when the temperature goes to zero, so does the average number of photons. In addition to the photon number in the bath, the master equation also includes the coupling rate Γ to the environment, the pure dephasing rate Γ_ϕ and the *Linbladian super operator*

$$\mathcal{D}\left[X\right]\rho = X\rho X^\dagger - \frac{1}{2}X^\dagger X\rho - \frac{1}{2}\rho X^\dagger X. \tag{2.37}$$

The second term in the master equation governs both the decay of excitations into the bath via both spontaneous and stimulated emission and corresponds to both *relaxation* and *dephasing* of the system. The relaxation is described by the diagonal terms in the density matrix and relates to the state population. In contrast, dephasing corresponds to the decay of the off-diagonal terms and the name comes from the fact that these elements contain the phase information of the state [12]. The third term governs thermal excitations i.e. energy absorption from the bath. However, because most experiments are performed close to $T = 0$ one often sets $n = 0$ resulting in that this term vanishes. The final term only leads to dephasing at the pure dephasing rate Γ_ϕ. In summary, the dissipators in the master equation results in the process of *decoherence* corresponding to the loss of information.

We are now equipped with the tools to describe open quantum systems such as the case of a qubit coupled to a waveguide and can move on to describing the interactions between the elements used in this thesis.

2.2.2 Qubit-qubit interaction

The initial interaction of interest is that between two transmons capacitively coupled to each other. For such a combined system the Hamiltonian takes a similar form to that of the famous Jaynes-Cummings Hamiltonian [33]

$$\mathcal{H} = \sum_{i=1}^{2} \frac{\omega_i}{2}\sigma_{z,i} + g\left(\sigma_1^+\sigma_2^- + \sigma_2^+\sigma_1^-\right). \tag{2.38}$$

where we recognize the sum over the individual transmon Hamiltonian but with an included coupling term. The coupling strength g of this term is proportional to the coupling capacitance between the qubits. Additionally, we note that $\sigma_j^{\{+,-\}}$ corresponds to the raising and lowering operators for the transmon which for a TLS can be defined as $\sigma^+ = |e\rangle\langle g|$ and $\sigma^- = |g\rangle\langle e|$. The coupling part of this Hamiltonian contains terms proportional to $\sigma_i^\pm\sigma_j^\mp$ which corresponds to an excitation exchange between the qubits. When the two qubits are resonant $\omega_1 = \omega_2 = \omega_q$ the Hamiltonian can be diagonalized by introducing two new modes that we call S and A [19]. By defining the raising and lowering operators as $\sigma_{S,A}^\pm = \frac{1}{\sqrt{2}}\left(\sigma_1^\pm \pm \sigma_2^\pm\right)$ and similarly for the other operators, a substitution of these into the Hamiltonian yields

$$\mathcal{H} = \frac{\omega_S}{2}\sigma_{z,S} + \frac{\omega_A}{2}\sigma_{z,A}. \tag{2.39}$$

This Hamiltonian we note corresponds to that of two uncoupled transmons with mode frequencies $\omega_{S,A} = \omega_q \pm g$. These two modes are usually referred to as the symmetric mode and antisymmetric mode which referees to the phase relation between the two coupled transmons. Furthermore, they are also sometimes termed bright and dark modes [60] because of how they interact with a coupled waveguide, something that will become evident in the next section.

2.2.3 Waveguide-qubit interaction

The second interaction of interest is that between a qubit and the field inside of a waveguide. As previously mentioned, the reduced dimensionality of the waveguide (compared to a three dimensional cavity QED system) can give rise to strong light-matter interactions [38]. The dynamics between the electromagnetic field inside of the waveguide when coupled to a qubit is described by the master equation 2.36 but we have yet to express the governing Hamiltonian.

In accordance with the second quantization of the electromagnetic field, the quantized field Hamiltonian is the same as for an infinite number of harmonic oscillators [12]. When only taking a *single mode* of the field into account, the interaction between the qubit and that mode can be described with the Hamiltonian

$$\mathcal{H} = \frac{\omega_0}{2}\sigma_z + J\left(\sigma_- a^\dagger + \sigma_+ a\right). \tag{2.40}$$

where ω_0 is the qubit frequency. In the derivation of this Hamiltonian found in [12], the dipole approximation and the rotating wave approximation has been used. For the actual case when the full continuum of modes is taken into account the interested reader is referred to Blais et.al. [26]. The first of these approximations assumes that the wavelength of the field is much longer than the interaction range while the second neglects all fast rotating terms and is only valid when the coupling strength $J << \omega$. The first term in this Hamiltonian we note correspond to that of an uncoupled transmon while the other describes the interaction between the transmon and the field and conserves the number of excitations.

If the qubit is periodically driven by light with a constant field amplitude, the Hamiltonian can be rewritten as [39]

$$\mathcal{H} = \frac{\omega_0}{2}\sigma_z + \Omega\sigma_x. \tag{2.41}$$

Here $\sigma_x = \sigma^+ + \sigma^-$ and Ω is the so called $Rabifrequency$, which is rate at which the state of the qubit is driven by the incoming field and is given by [19]

$$\Omega = 2\sqrt{\frac{\Gamma P}{\hbar\omega}}. \tag{2.42}$$

This frequency depend on the applied microwave power P, the frequency ω and the coupling rate $\Gamma = \Gamma_r + \Gamma_{nr}$. The radiative coupling rate Γ_r corresponds to the coupling to the waveguide (thus the excitation being radiated into the waveguide) and depend on the capacitive coupling and the qubit frequency. In contrast, the non-radiative decay Γ_{nr} instead relates to the coupling to the environment, thus information being lost and not radiated back into the waveguide.

At this point it is also of interest to investigate the case of the interaction between the waveguide and two coupled transmons. From equation 2.41 and 2.38 we can construct this Hamiltonian as [19]

$$\mathcal{H} = \sum_{j=1}^{2}\left[\frac{\omega_j}{2}\sigma_{z,j} + \Omega_j\sigma_{x,j}\right] + g\left(\sigma_1^+\sigma_2^- + \sigma_2^+\sigma_1^-\right) \tag{2.43}$$

and by moving into the symmetric/antisymmetric basis as we did for the coupled transmon case (equation 2.39), we find

$$\mathcal{H} = \sum_{k=\{S,A\}} \frac{\omega_k}{2}\sigma_{z,k} + \Omega_k\sigma_{x,k} \tag{2.44}$$

where the driving rate now correspond to $\Omega_{S,A} = \frac{1}{\sqrt{2}}\left(\Omega_1 \pm \Omega_2\right)$. Therefore we note that in the case $\Omega_1 = \Omega_2$ the antisymmetric mode is not driven at all (it becomes decoupled from the waveguide) while the symmetric mode experiences an enhanced driving rate.

2.3 Light-matter interaction

The main method of studying the qubit in this thesis is by sending in light through the waveguide and observing the output. By probing the system in such a manner one can characterize the system parameters and determine the internal dynamics taking place. The light matter interaction between this incoming field and the qubit, results in so called *dressed* energy levels of which the effects can be observed when measuring the power spectral density (PSD) of the output signal. In this section we therefore begin by introducing input-output theory before proceeding to describing the dressed state picture.

2.3.1 Input-output theory

The purpose behind input-output theory is to predict the mode amplitude of the output field a_{out} coupled to an atom, given that the input field a_{in} and the master equation governing the internal dynamics is known. In the case of a coherent probe field we also write $\alpha_{in,out} = \langle a_{in,out} \rangle$. In this thesis we consider a qubit coupled to the end of a waveguide and use input-output theory to characterize the measured reflection coefficient, defined as [40]

$$r = \frac{\alpha_{out}}{\alpha_{in}}. \tag{2.45}$$

This expression is known as a scattering parameter and can be probed in spectroscopy using a vector network analyzer (VNA). If the input field do not interact with anything, then clearly $\alpha_{out} = \alpha_{in}$ and the reflection would be unity. However, if the waveguide is not empty then the interaction Hamiltonian between the field and e.g. a qubit will determine the equation of motion for the output mode resulting in a potential change of the reflection. The situation of interest for this thesis is depicted in Figure 2.5 where the incoming field with frequency ω_d is scattered at a qubit with a transition frequency ω_0.

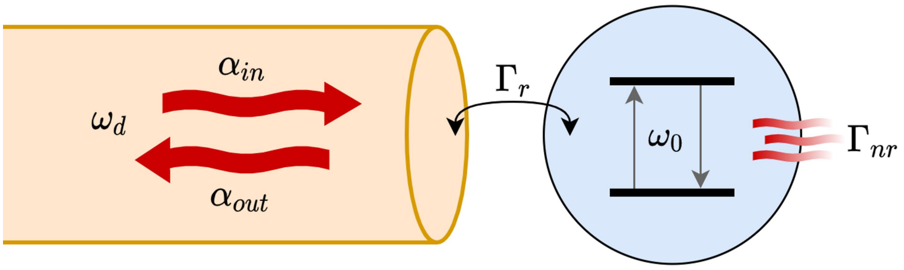

Figure 2.5: Illustration of the setup relevant to this thesis where a qubit with transition frequency ω_0 is coupled to the end of a waveguide. The field with frequency ω_d inside of the waveguide has an incoming and outgoing component α_{in} and α_{out}. The non-radiative coupling to the environment occurs at the rate Γ_{nr} and results in that information is lost to the environment. In contrast, the radiative coupling rate Γ_r to the waveguide sends the information back into the waveguide.

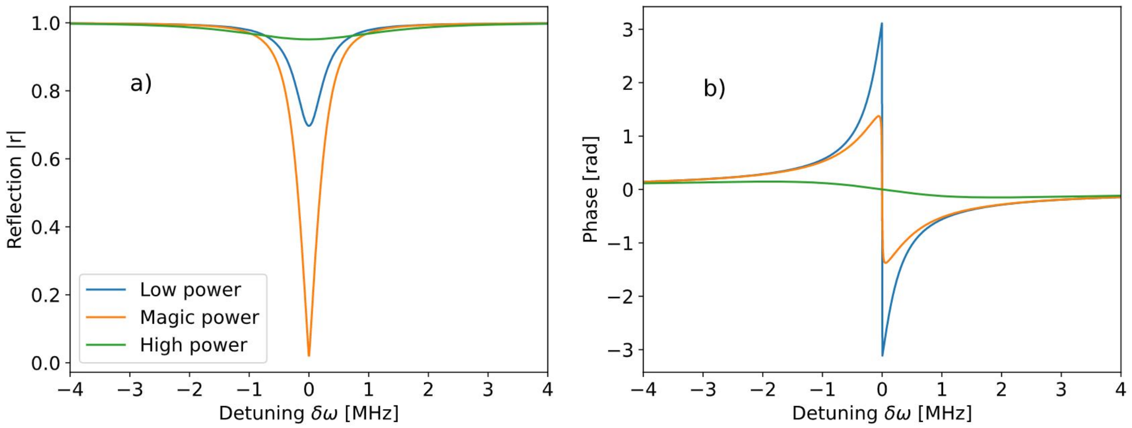

Figure 2.6: a) Magnitude of the theoretically expected reflection (equation 2.47) from a qubit with resonance frequency at 5 GHz. The coupling parameters were arbitrarily chosen and the driving rate Ω calculated as per equation 2.42. At the magic power we have coherent scattering and thus complete destructive interference. b) The phase response of the reflection coefficient at the same input powers as in a).

According to input-output theory for such a situation, the relationship between the incoming and outgoing fields are described in detail in [40] and is written as

$$\alpha_{out} = \alpha_{in} + \sqrt{\frac{\Gamma}{2}} \left\langle \hat{\sigma}^- \right\rangle . \tag{2.46}$$

where $\alpha_{in} = \frac{\Omega}{2\sqrt{\Gamma}}$. Therefore, since the parameters for the input field are generally known (such as power and frequency), the only part needed for a theoretical expression of the reflection is the expectation value of the lowering operator $\langle \hat{\sigma}^- \rangle$. This is given by solving the systems master equation in steady state and extracting the off-diagonal element $\rho_{10} = \langle \hat{\sigma}^- \rangle$. This is rigorously done in the supplementary information of Yong *et al.* [41] and yields the reflection coefficient

$$r = 1 - \frac{i\Gamma_r\Gamma_1 \left(\Delta - i\Gamma_2\right)}{\Omega^2\Gamma_2 + \Gamma_1 \left(\Delta^2 + \Gamma_2^2\right)}. \tag{2.47}$$

Here $\Gamma_1 = \Gamma_r + \Gamma_{nr}$ and $\Gamma_2 = \frac{\Gamma_r + \Gamma_{nr}}{2} + \Gamma_\phi$ and $\Delta = |\omega_d - \omega_0|$ represents the detuning between the qubit and the driving field.

When a coherent signal is sent into a waveguide coupled to a qubit the incoming field can either get reflected or it can interact with the qubit. When the field interacts it will be absorbed and then reemitted from the qubit either coherently or incoherently with respect to the incoming field. While the incoherent scattering has a random phase, the coherently scattered radiation has opposite phase to the incoming field and can thus destructively interfere with the incident field [47]. However, the the response of the qubit is strongly dependent on the power of the incoming field and can be studied using e.g. a VNA which can record the scattering parameter $S_{11} = r$ (see Figure 2.6). This parameter consists of a complex number and thus include both magnitude and phase information about the scattering process. At high input power the qubit is completely saturated (equal populations in ground and excited state) meaning that the light is scattered incoherently resulting in no destructive interference and thus no observable change can be seen in the reflection (r = 1 even at the resonance frequency). Lowering the power results in that an increase in the coherent scattering and a dip in the magnitude can be observed around the resonance frequency in combination with a phase change. At the input power corresponding to exactly $\Omega = \frac{\Gamma_r}{\sqrt{2}}$, we have complete coherent scattering and therefore full destructive interference resulting in that the reflection at resonance frequency goes to zero and we get a full π phase shift. This power we therefore call the *magic power*, since we here have full destructive interference. Lowering the power even further will however result in fewer excitations and thus again an increase in the coherent scattering and a smaller visible response in the measured scattering parameter S_{11}.

2.3.2 Dressed state picture

As seen in the previous section the reflection coefficient depends on the detuning Δ between the field and the transition frequency of the qubit. The reason behind this is that in the presence of an electromagnetic field the energy structure of the qubit will change. In fact, the field and the qubit will merge into hybridized quantum states resulting in so called *dressed* energy levels [26,42]. When considering a single mode inside of the waveguide, the combined system contains two types of quantum numbers, n which indicates the number of photons and g or e representing the ground and excited state of the TLS. The dressed eigenstates which energies are separated by Δ, can then be divided into manifolds

$$\mathcal{E}(n) = \{|g, n+1\rangle, |e, n\rangle\} \tag{2.48}$$

that contain two uncoupled states but with an equal number of excitations [12]. In the case of a sufficiently strong coherent pump field being sent into the waveguide, the energy structure of the TLS will change even further. The energy levels within a manifold are split into levels where the energy difference corresponds to the driving rate Ω_R which we know from the previous section, is proportional to the strength of the pump field and the effect this has on the dressed energy levels can be seen in Figure 2.7. The new eigenstates for the coupled field-qubit system in the $\mathcal{E}(n)$ can be expressed as

$$|\pm, n\rangle = \frac{|g, n+1\rangle \pm |e, n\rangle}{\sqrt{2}} \tag{2.49}$$

with the energy difference of $\Omega = \sqrt{\Delta^2 + \Omega_R^2}$ meaning that on resonance, the energy difference corresponds to the driving rate Ω_R [42].

One remarkable property of the dressed energy levels appears in the resonance fluorescence spectrum of the TLS. When measuring the power spectral density (PSD) of the output field the spectrum contains one central peak at the resonance frequency ω_0 in addition to two sidebands. Together they form the famous Mollow triplet. In the case of a qubit at the end of a waveguide the theoretical expression for the PSD

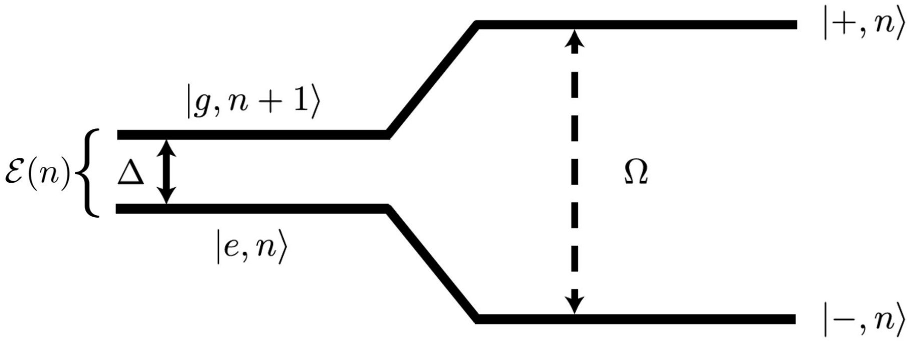

Figure 2.7: Depiction of the dressed states in the $\mathcal{E}(n)$ manifold. Because of the coupling between the field and the TLS it causes the uncoupled levels $|g,n+1\rangle$ and $|e,n\rangle$ to turn into the dressed states $|\pm,n\rangle$ separated by $\Omega = \sqrt{\Delta^2+\Omega_R^2}$. Figure modified from [12]

has been derived in [12, 61] and reads

$$S_{\mathrm{i}}(\omega) \approx \frac{1}{2\pi}\frac{\hbar\omega_0\Gamma_{\mathrm{r}}}{4}\left\{\frac{\Gamma_{\mathrm{s}}}{(\Delta+\Omega)^2+\Gamma_{\mathrm{s}}^2}+\frac{2\Gamma_2}{\Delta^2+\Gamma_2^2}+\frac{\Gamma_{\mathrm{s}}}{(\Delta-\Omega)^2+\Gamma_{\mathrm{s}}^2}\right\} \tag{2.50}$$

where $\Gamma_s = (\Gamma_1+\Gamma_2)/2$. The reason behind the three peaks can be understood when taking the possible transitions between manifolds into account as displayed in Figure 2.8. In this example we have two possible transitions at the frequency ω_0 (red arrows) from the $\mathcal{E}(n+1)$ manifold to $\mathcal{E}(n)$ resulting in the middle peak of the Mollow triplet. In addition to these we also have one allowed transition at both $\omega_0 \pm \Omega$ corresponding to the blue and green arrows respectively which gives rise to the two sidebands.

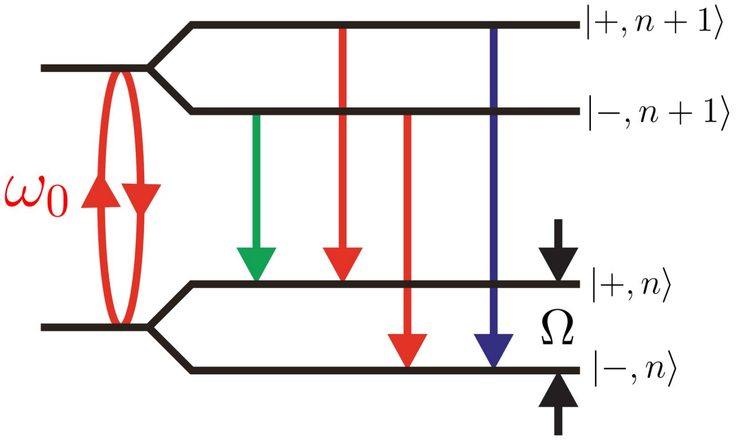

Figure 2.8: Illustration of the possible transitions in the dressed state between the two manifolds $\mathcal{E}(n+1)$ and $\mathcal{E}(n)$. The bare states has an energy difference corresponding to ω_0 and the dressed states are split with a difference equal to Ω.

2.3.3 Dressed qubits

The concept of dressed energy levels between a field and an atom can also be extended to that of two coupled qubits. In the review by Blais *et al.* [26], they show that the linear part of the interaction Hamiltonian between a resonator (LC-circuit) coupled to a TLS when expressed using creation and annihilation operators reads

$$\mathcal{H}_L = \omega_r a^\dagger a + \omega_q b^\dagger b + J\left(b^\dagger a + b a^\dagger\right). \tag{2.51}$$

Here $a^\dagger, a$ and $b^\dagger, b$ correspond to the bosonic creation and annihilation operators for the resonator ω_r and the qubit ω_q respectively. We note that because the first term in this expression which corresponds to the resonator Hamiltonian has the same form as the second term which describes the TLS, we can replace the resonator related parts to that of a second qubit and exchange the coupling strength J with the coupling strength g between the two qubits. We can therefore express the interaction Hamiltonian between the two qubits as

$$\mathcal{H} = \omega_{q1} b_1^\dagger b_1 + \omega_{q2} b_2^\dagger b_2 + g\left(b_1^\dagger b_2 + b_2^\dagger b_1\right). \tag{2.52}$$

and proceed with its diagonalization in the same manner as was done for equation 2.51 using the Bogoliubov transformation. This results in the Hamiltonian

$$\mathcal{H} = \tilde{\omega}_{q1} b_1^\dagger b_1 + \tilde{\omega}_{q2} b_2^\dagger b_2. \tag{2.53}$$

where the new dressed frequencies are

$$\tilde{\omega}_{q1} = \frac{1}{2}\left(\omega_{q1} + \omega_{q2} - \sqrt{\Delta^2 + 4g^2}\right), \tag{2.54}$$

$$\tilde{\omega}_{q2} = \frac{1}{2}\left(\omega_{q1} + \omega_{q2} + \sqrt{\Delta^2 + 4g^2}\right). \tag{2.55}$$

As expected we note that at resonance when the two qubit frequencies are equal $\omega_{q1} = \omega_{q2} = \omega_q$, we get the same energy difference of $2g$ between the two modes as we found when discussing the qubit-qubit interaction in section 2.2.2.

2.4 The quantum thermal machine

The classical law of heat conduction within a material was stated by Fourier in 1822 and is expressed as [62]

$$J = -\kappa \nabla T. \tag{2.56}$$

This expression relates the current of heat J to the thermal conductivity κ of the material and the heat gradient. In this thesis however, we focus on an equivalent heat flow but in quantum mechanical systems. In particular the system of interest is that of two coupled qubits with two independent waveguides (thermal baths) coupled to the symmetric (SM) and antisymmetric (ASM) modes respectively. These waveguides therefore effectively see a qubit as described and illustrated in the introduction and Figure 1.3. In this section we combine the tools we have acquired so far in order to describe the heat currents in our system and how the added noise affects these flows.

2.4.1 Heat flow

From the previous section we recall that the Hamiltonian of two coupled qubits both with bare frequencies ω can be written as

$$\mathcal{H} = \omega b_1^\dagger b_1 + \omega b_2^\dagger b_2 + g\left(b_1^\dagger b_2 + b_2^\dagger b_1\right) \tag{2.57}$$

where the coupling term preserves the number of excitations and describes the "hopping" of excitations between the qubits. In addition to the coupled qubits our system also includes two waveguides which couple to the symmetric and antisymmetric mode respectively. The dynamics of the system is therefore treated in the framework of the quantum optical master equation and can for this double-waveguide scenario be written as

$$\dot{\rho} = \mathcal{L}\rho = -i[H,\rho] + \mathcal{L}_s\rho + \mathcal{L}_a\rho + \frac{\Gamma_\phi}{2}\mathcal{D}\left[\sigma_z\right]\rho. \tag{2.58}$$

Here the terms $\mathcal{L}_S\rho$ and $\mathcal{L}_A\rho$ contains the local dissipation taking place between the waveguides coupled to the SM and ASM respectively. As described in section 2.2.1, these can be expressed in terms of super operators

$$\mathcal{L}_{j=\{s,a\}}\rho = \Gamma_j(n_j+1)\mathcal{D}\left[\sigma_j^-\right]\rho + \Gamma_j n_j\mathcal{D}\left[\sigma_j^+\right]\rho. \tag{2.59}$$

The raising and lowering operators σ_j^+ and σ_j^- are expressed in the SM and ASM basis meaning that in terms of terms of the bare qubits they are $\sigma_{s,a}^\pm = \frac{1}{\sqrt{2}}\left(\sigma_1^\pm \pm \sigma_2^\pm\right)$ (and similarly for σ_z) as described in section 2.2.2.

The mean heat current flowing between the two waveguides can be obtained by following the arguments in [45]. In steady state, the time derivative of the energy expectation value will vanish

$$\frac{d}{dt}\langle H\rangle = \mathrm{Tr}\left(H\mathcal{L}\rho\right) = 0. \tag{2.60}$$

For our system, heat currents can flow in and out of the two waveguides but energy can also be exchanged through the dephasing channel. One can therefore view this channel as a third waveguide acting as thermal bath longitudinally coupled to one of the qubits. By inserting the master equation into 2.60 one would expect the contributions of all three heat baths to be non-zero but cancel each other out. This should amount to a positive heat current from the hot bath coupled to the SM and a negative current into the cold bath coupled to the ASM. The net heat flow into the symmetric or antisymmetric waveguide can thus be written as

$$J_{i=\{s,a\}} = \mathrm{Tr}\left(H\mathcal{L}_i\rho\right) \tag{2.61}$$

with the heat flow from the dephasing channel similarly expressed as

$$J_{\text{dephasing}} = \mathrm{Tr}\left(H\frac{\Gamma_\phi}{2}\mathcal{D}\left[\sigma_z\right]\rho\right). \tag{2.62}$$

By calculating the steady state solution for the systems master equation 2.58 we get the net heat currents into the two waveguides as

$$J_{\{s,a\}} = \frac{\hbar(n_a - n_s)\Gamma_a\Gamma_s\Gamma_\phi(g \pm \omega_0)}{\Gamma_s\Gamma_\phi + \Gamma_a(2\Gamma_s + \Gamma_\phi)} \tag{2.63}$$

with ω_0 being the bare qubit frequency for the two identical qubits. Similarly we also obtain the heat flow from the dephasing line

$$J_{\text{dephasing}} = -\frac{2g\hbar(n_a - n_s)\Gamma_a\Gamma_s\Gamma_\phi}{\Gamma_s\Gamma_\phi + \Gamma_a(2\Gamma_s + \Gamma_\phi)}. \tag{2.64}$$

As expected we note that $J_a + J_s + J_{\text{dephasing}} = 0$ meaning that energy is conserved. In addition to the heat flows, the occupation numbers of the two modes can be extracted from the diagonal in the density matrix which turns out to be

$$P_s = \frac{(n_a\Gamma_a + n_s\Gamma_s)\Gamma_\phi + 2n_s\Gamma_s\Gamma_a}{\Gamma_s\Gamma_\phi + \Gamma_a(2\Gamma_s + \Gamma_\phi)} \tag{2.65}$$

$$P_a = \frac{(n_a\Gamma_a + n_s\Gamma_s)\Gamma_\phi + 2n_a\Gamma_s\Gamma_a}{\Gamma_s\Gamma_\phi + \Gamma_a(2\Gamma_s + \Gamma_\phi)}. \tag{2.66}$$

The difference in the populations can thus be calculated as

$$\Delta P = \frac{2(n_s - n_a)\Gamma_s\Gamma_a}{\Gamma_s\Gamma_\phi + \Gamma_a(2\Gamma_s + \Gamma_\phi)} \tag{2.67}$$

which we see for zero dephasing results in $\Delta P = n_s - n_a$. This intuitive answer without any dephasing is expected since in such a case at thermal equilibrium, one would imagine that the populations would be $P_s = n_s$ and $P_a = n_a$. This can also be verified by solving the master equation in steady state and once again extract the diagonal elements resulting in $P_s = (1 - n_a)n_s \approx n_s$ and $P_a = (1 - n_s)n_a \approx n_a$ (for small occupation numbers).

By looking at the populations it is therefore true that in the absence of dephasing the two modes thermalize separately while in the case of dephasing there exists a competition between separate thermalization and population equilibration due to the dephasing. Therefore we now proceed in the next section by describing how applied noise relates to dephasing and what effect this has on an individual qubit.

2.4.2 Classical noise environment

With the aim of describing the effects which a classical noise environment has on a transmon qubit we start from the quantity that governs the evolution of a single flux tuneable qubit, its Hamiltonian

$$\mathcal{H}_0 = -\frac{\omega_0(\phi)}{2}\hat{\sigma}_z. \tag{2.68}$$

Here we recall section 2.1.2 where the flux dependence of the bare qubit frequency was derived as

$$\omega_0 = \sqrt{8E_CE_J\left|\cos\left(\pi\frac{\Phi}{\Phi_0}\right)\right|} - E_C. \tag{2.69}$$

The charging energy E_C and Josephson energy E_J can for higher temperatures be subjugated to small fluctuations but for the lower temperatures which are of interest in this thesis, these fluctuations can be assumed negligible. Therefore these parameters are fixed after fabrication of the qubit and its frequency is thus only parametrized by the external flux Φ. This flux can however be affected by noise resulting in that we can express the flux as $\Phi(t) = \Phi + \delta\Phi(t)$ where we have included small fluctuations around some working point value. In order to see how this noise affect the qubit we can expand the Hamiltonian around the working point value as [44]

$$\mathcal{H} = \mathcal{H}_0 + \frac{d\mathcal{H}_0}{d\Phi}\delta\Phi(t) + \frac{1}{2!}\frac{d^2\mathcal{H}_0}{d\Phi^2}\delta\Phi(t)^2 + \mathcal{O}\left(\delta\Phi(t)^3\right). \tag{2.70}$$

If we assume that the fluctuations are small in relation to the working point value, we can disregard terms of order $(\delta\Phi(t)^2)$, resulting in an approximation of the Hamiltonian given by

$$\mathcal{H} = -\frac{1}{2}\left(\omega_0 + \frac{d\omega_0}{d\Phi}\delta\Phi(t)\right)\sigma_z = -\frac{(\omega_0 + \delta\omega(t))}{2}\sigma_z. \tag{2.71}$$

As expected we see that the flux noise results in fluctuations of the transition frequency $\omega(t) = \omega_0 + \delta\omega(t)$. The master equation governing the dynamics of such a system is given by [43]

$$\dot{\rho} = -\frac{i}{2}\omega_0\left[\sigma_z, \rho\right] + \frac{\gamma_\phi(t)}{2}\left(\sigma_z\rho\sigma_z - \rho\right) \tag{2.72}$$

where we note the dissipator depending on the pure dephasing. It turns out as shown in [19], that for white noise with amplitude A the pure dephasing rate can be expressed as

$$\gamma_\phi(t) = \pi A\left(\frac{d\omega_0}{d\Phi}\right)^2 \tag{2.73}$$

Therefore the dephasing rate depends upon both the amplitude of the noise as well as the sensitivity of the bare frequency in regards to the magnetic flux.

This concludes this chapter and we now move on to a description of the device, the experimental setup and the measurements performed in this thesis.

3

Methods

In the previous chapter we introduced the theory governing the physics behind the elements and important concepts related to this thesis. We therefore begin this chapter by describing the device used as a quantum thermal machine. Because the device used had been designed previous to this project by Dr. Aamir Ali, the specifics regarding the design choices and fabrication will be omitted. However, since our device closely resembles the device presented by Kowshik [47], the curious reader is referred to his thesis. After introducing the device, an overview of the experimental setup will be given followed by the different measurements performed throughout this project.

3.1 Experimental setup

In this section the cryogenic setup used for all the experiments will be presented in conjunction with the coupling scheme connecting to the device. Also, the specifics regarding the device used as a quantum thermal machine will be elaborated upon.

3.1.1 Our device

The device studied in this thesis is very similar to that presented in [47]. It consists of two flux-tuneable qubits with the capacitive plates marked in blue and green in Figure 3.1. Each qubit comes with its own flux-line and by applying a DC-voltage to these lines the resulting magnetic flux ϕ threading the SQUIDs enables one to individually tune the bare frequencies of the two qubits. Additionally these qubits are capacitively coupled to each other with a coupling strength g resulting in that the two qubits hybridizes and form dressed energy levels as seen in Figure 3.2. Studying the symmetry (that is the parity) of the modes occupying these dressed energy levels it turns out that the lowest excited level is antisymmetric while the other is symmetric. When taking into account the oscillations within our circuit we see that the symmetric waveguide (SWG) couples to the capacitor plates where the voltage is in-phase. The antisymmetric waveguide (ASWG) on the other hand, couples to the plates where the voltage is out-of-phase. Thus this coupling scheme is engineered so that transitions involving the symmetric mode (SM) is predominantly over-couples to the SWG while the antisymmetric mode (ASM) mostly over-couples to the ASWG. In essence we therefore have symmetry selective decay into the two respective waveguides.

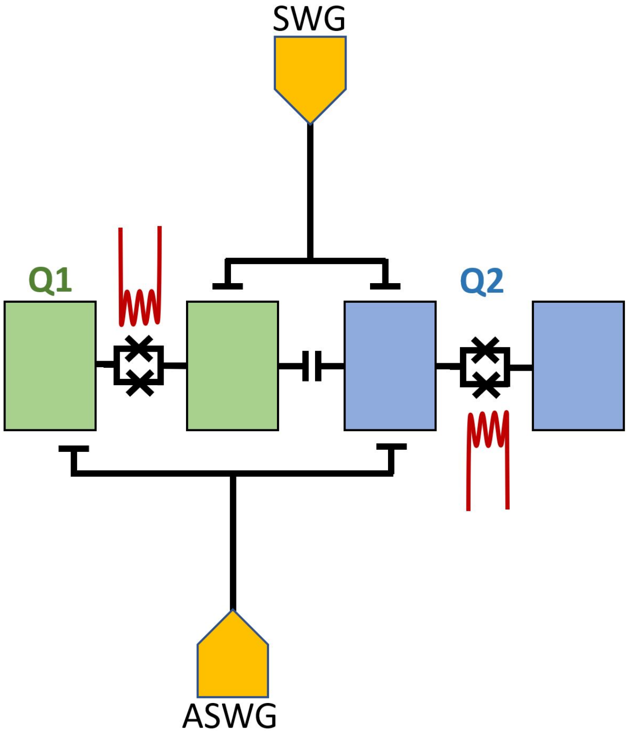

Figure 3.1: Illustration of the device studied in this thesis. Two flux-tuneable qubits are capacitively coupled, each having its own flux-line. The two waveguides labeled SWG and ASWG couples to the symmetric and antisymmetric modes respectively.

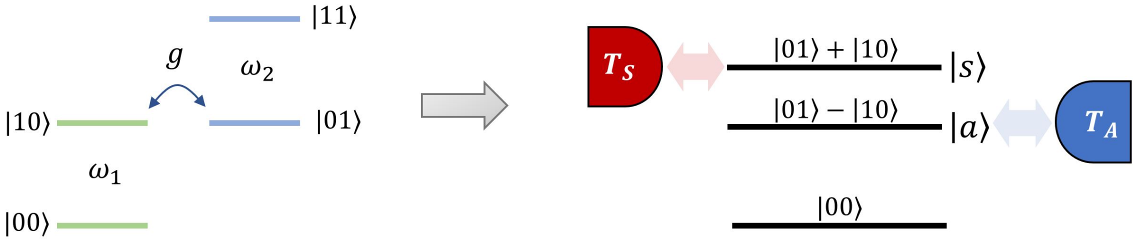

Figure 3.2: The energy levels of the two qubits with coupling strength g hybridize resulting in dressed energy levels. In the right part of the figure the first two higher energy levels are illustrated. Because of the coupling scheme we then get symmetry selective decay into the two respective waveguides.

While the details of the fabrication process are to be omitted the recipe closely follows that discussed by J.J.Burnett et.al. [63]. The fabricated chip is bonded onto a PCB with aluminium wirebonds and connected to the lines of the cryostat. The device along with a cutout of the SQUID is shown in figure 3.3.

3.1.2 Cryogenic setup

The experiments performed throughout this project was performed in a cryostat, also known as a dilution refrigerator. A cryostat enables us to reach extremely low temperatures and thus allowing for experiments in cQED where superconductivity is

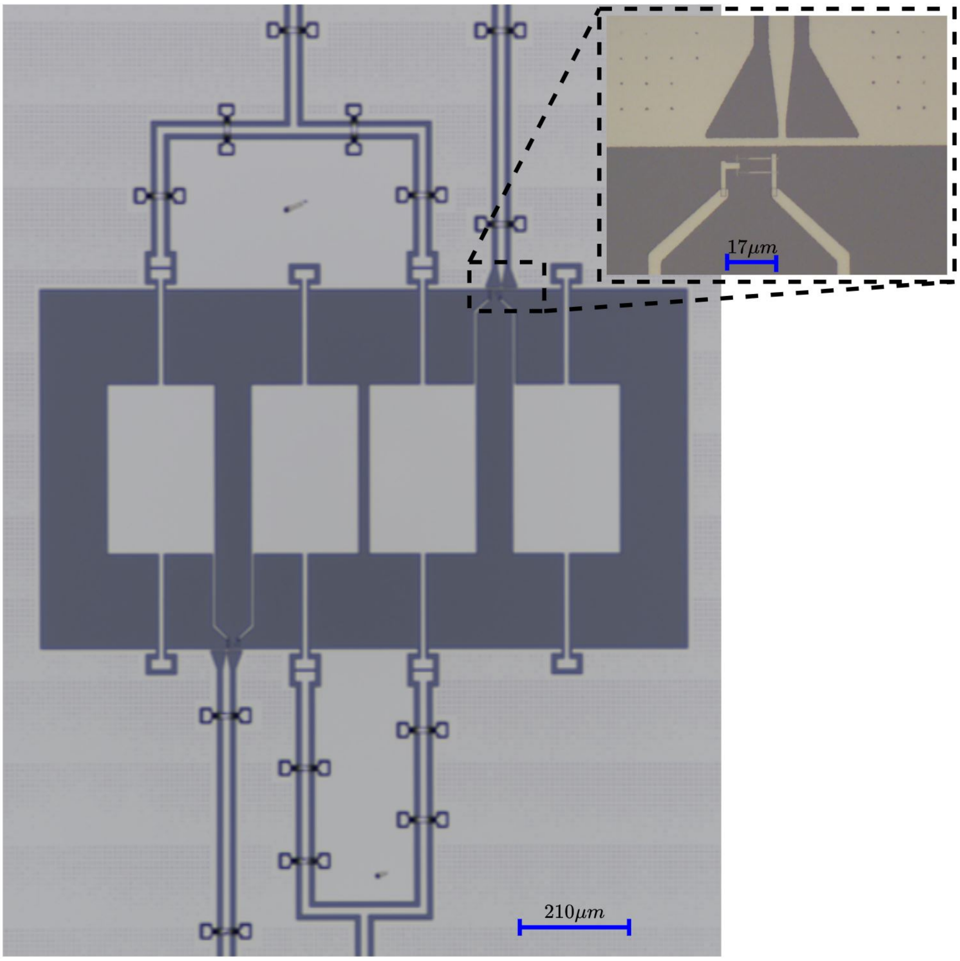

Figure 3.3: Image of the fabricated device including a cutout of the connection between the flux line and the SQUID. Note the so called air-bridges connecting different regions which ensures that there is no voltage difference between the outer region and the regions encircled by the waveguide/flux lines.

essential. Furthermore, when investigating quantum mechanical components such as qubits, the temperature must also be very low in order to improve e.g. the lifetimes of the qubits. The low temperatures also results in that the thermal background in the GHz range (where our frequency points of interest lies) becomes negligible. In addition to providing a low temperature environment a cryostat also provides good shielding from electromagnetic fields in the vicinity which could otherwise interfere with the device.

The cryostat used in this thesis is the BlueFors LD Dilution Refrigerator System which was operated at a temperature near 9 mK. The specifics behind how such low temperatures can be reached can be found on BlueFors website [46] but the main principle involves the mixing of the two Helium isotopes ^{4}He and ^{3}He. However, in order to connect room temperature electronics to the device placed in an environment of a few mK, the cryostat has several temperature stages. One can then probe the device through wires connecting the room temperature environment and the device. The wiring diagram along with the six different temperature levels are shown in Figure 3.4 together with an image of the cryostat without any of the shielding. Before proceeding and with a short explanation of the main wiring components we introduce the so-called Traveling wave parametric amplifier (TWPA) which is a quantum limited amplifier and a very useful tool in experiments involving weak signals [64].

Classical low-noise semiconductor-based amplifiers such as the HEMT amplifier in the wiring diagram, adds noise on top of the input signal [47]. This noise can overwhelm the often very small signal coming from a quantum system, which is the case in this thesis where we monitor signals that average out to be less than a single photon! Fortunately, there is a way to reduce this noise by using quantum-limited amplifiers which only adds the minimum possible noise of half a photon (at the signal frequency) dictated by quantum mechanics. This means that in the purely ideal case, the signal-to-noise ratio (SNR) corresponds to a factor of two where half a photon is added to the incoming half photon. In this thesis we are using a single *traveling wave parametric amplifier* (TWPA) constructed by the company VTT, Finland. The concept behind the TWPA is a coplanar waveguide with a centre conductor consisting of Josephson based elements allowing for a 3-wave mixing process where the energy from a pumping microwave signal is transferred to the weak incoming signal [48]. In addition to the pump tone, the TWPA also requires a connection to a DC line providing a magnetic flux bias. In essence the TWPA provides a broadband quantum noise limited gain to the signal. The signal which now has a larger amplitude can then be sent into a classical amplifier without any significant degradation in the SNR, allowing for better quality data.

Apart from the TWPA in the wiring diagram, we note the use of several attenuators on the input lines going to the devices and the TWPA. The purpose of these are to prevent thermal photons on that temperature level to reach the TWPA or device. Another crucial component is the circulator which is a non-reciprocal microwave component with three ports. The input signal passes through to the device while the scattered signal is prevented from traveling back into the input line and instead goes into the output line. The bias tee is a component allowing us to combine DC with an RF signal. This is needed in order both send in DC to the flux lines of the qubits but also sending in RF-noise through the flux line in order to induce dephasing. The remaining components consist of different types of filters, a directional coupler which adds two signals and isolators that only allows signals to travel in one direction (it works as a unidirectional attenuator).

At room temperature the DC lines connected to the two flux lines of the device and the TWPA flux were connected to three separate ports on a floating voltage source. The connections to the other lines did in turn depend on what type of measurement was being performed. Therefore we proceed to the next section where a description of these connections are presented along with the different measurements performed throughout this project.

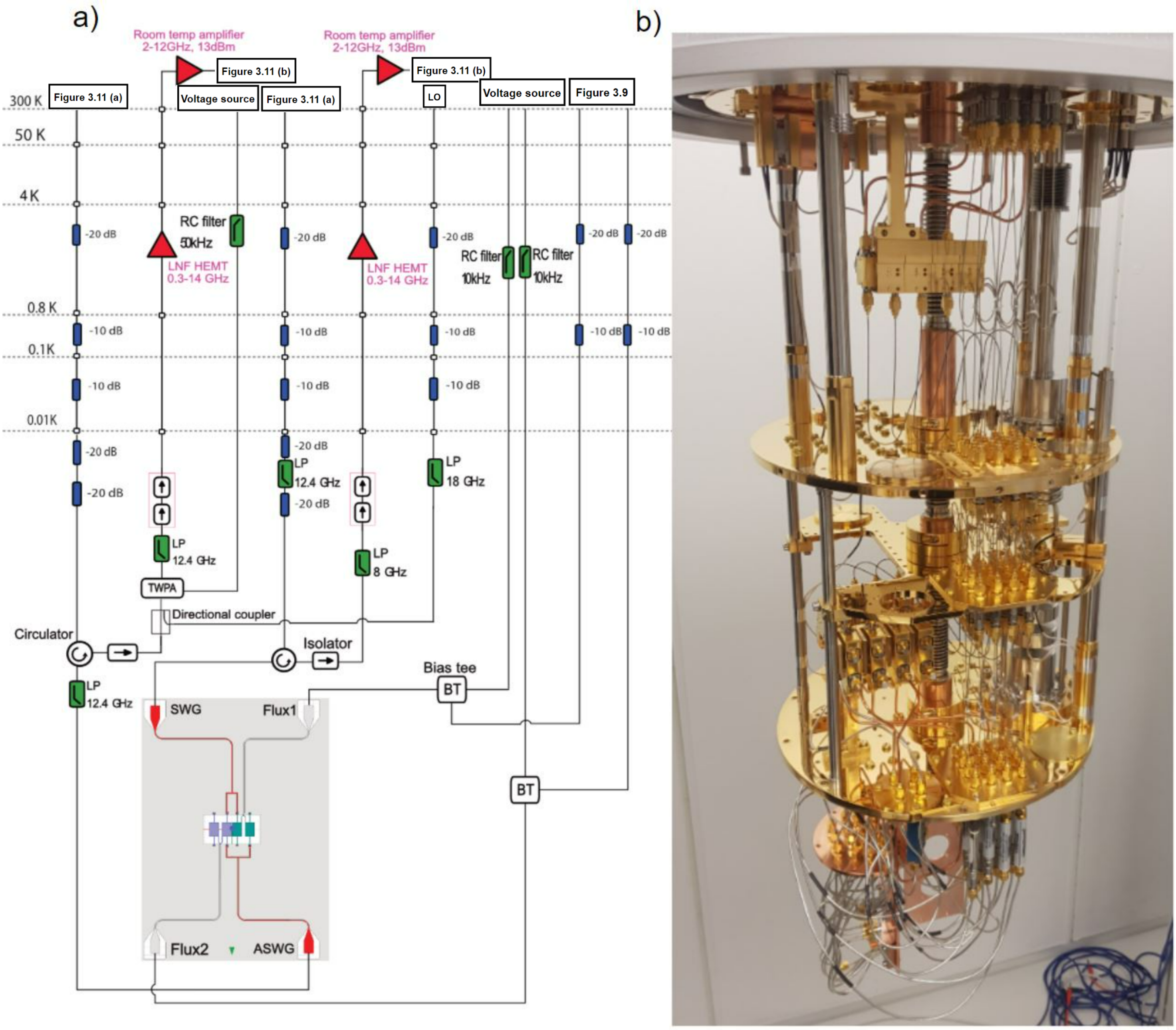

Figure 3.4: a) Wiring diagram inside of the cryostat from room temperature through the temperature levels down to the device. b) Image of the cryostat with all shielding elements removed.

3.2 Characterization

Before the main experiments, involving measurements of heat flows could be performed, characterization of the system was necessary. The region where the qubits were completely hybridized, that is where the e.g. the SWG only coupled to the SM had to be found. Also, the TWPA connected in the output of the ASWG had to be properly calibrated in order to yield the maximum gain and least noise at the ASM frequency. Following this, the coupling rates between the modes and their respective waveguides was determined along with the effects of applied noise into one of the flux lines.

Many of these experiments was performed by probing the device in each of the waveguides and studying the reflection coefficient using vector network analyzer (VNA) in addition to a spectrum analyzer (SA). The input and output lines from the cryostat shown in Figure 3.4 were therefore connected to a VNA which also had a SA mode. The measurements and data collection was then preformed using Labber which is a general-purpose instrument control and lab automation software package. Through Labber, instrument specific drivers were developed, allowing for control of the instrument (in this case the VNA) through a virtual instrument. In addition to the VNA, several experiments also made extensive use of arbitrary waveform generators (AWG) and a digitizer (DIG), both utilizing uniquely developed Labber drivers.

3.2.1 Finding dressed state

Tuning the bare frequencies away from their initial values had a twofold motivation. The primary reason can be understood from equation 2.73 which describes the pure dephasing due to white noise. Because one cannot arbitrarily increase the amplitude of the applied noise in order to reach higher dephasing rates, the qubit has to be in a region where its bare frequency is sensitive to external flux. Therefore the bare frequencies need to be tuned away from the "sweet-spot" with no applied flux where $\frac{d\omega_0}{d\Phi}$ is small, to a region with a steeper slope. The secondary reason relates to how the two qubits were designed to have the same frequency resulting in that the combined system would be fully hybridized and e.g. the SWG would only couple to the SM without or with very low cross coupling to the ASM. However, small uncertainties in the fabrication process might not result in the two frequencies being equal. From equation 2.54 and 2.55 describing the dressed frequencies (which are what we actually observe through the waveguides) we see that the difference in the dressed frequencies are the smallest when the bare frequencies of the two qubits are equal, yielding $\tilde{\omega}_s - \tilde{\omega}_a = 2g$.

In section 2.1.2 we found that the bare frequency of a flux tuneable qubit depends on the magnetic flux ϕ (equation 2.25). In order to control this magnetic flux, a voltage is applied using a floating voltage source at the RC filter of the flux line. Here the fixed in-line resistance of 1.7 kΩ facilitates a constant current source to the flux line in the device, proportional to the applied voltage. This DC signal is then what controls the magnetic flux threading the SQUID. Therefore, before determining what applied flux was needed to reach a steep enough slope while having a fully hybridized system, the relation between applied voltage and the actual magnetic flux had to be found. A single flux line consisting of a small superconducting coil is expected to act primarily on the qubit it is nearest to but will through some finite cross-coupling also affect the other. In order to gain individual control over the qubits this cross-coupling in addition to the direct coupling strength had to be determined. One can therefore model the system as follows; each flux generating element $i = \{1, 2\}$ is controlled by some applied voltage V_i. This applied voltage is in turn linearly related to the flux experienced by the individual qubits through the mutual inductance matrix $M_{i,j}$. In addition to the flux generated by the user, the model should also include some potential environmental offset which we call ϕ_{ei}. For our device consisting of two flux tuneable qubits we can therefore model the flux as

$$\begin{pmatrix} \Phi_1 \\ \Phi_2 \end{pmatrix} = \begin{pmatrix} M_{11} & M_{12} \\ M_{21} & M_{22} \end{pmatrix} \begin{pmatrix} V_1 \\ V_2 \end{pmatrix} + \begin{pmatrix} \Phi_{e1} \\ \Phi_{e2} \end{pmatrix} \tag{3.1}$$

We can thus combine this with equation 2.54, 2.55 and 2.25 to write the full flux dependent model of the dressed frequencies as

$$\tilde{\omega}_{s,a}(\Phi) = \frac{1}{2}\left(\omega_{q1}(\Phi) + \omega_{q2}(\Phi) \pm \sqrt{\Delta^2 + 4g^2}\right) \tag{3.2}$$

$$\omega_{qi} \approx \sqrt{8E_{Ci}E_{Ji}\left|\cos\left(\frac{\pi}{\Phi_0}(m_{i*} \cdot \vec{V} + \Phi_{ei})\right)\right|} - E_{Ci} \tag{3.3}$$

where m_{i*} represents the ith row in the inductance matrix.

In section 2.3.1 we saw that by measuring the reflection coefficient $S_{11} = r$ at the so called magic power, a dip centered at the mode frequency becomes apparent when studying the magnitude of the reflection. In our setups these dips correspond to the mode frequencies of the SM and ASM and by sweeping the input power from the VNA their respective magic powers (when studied through their respective waveguides) were found and are presented in table 3.1.

Table 3.1: Characterization of parameters without any applied flux ($\phi/\phi_0 = 0$).

Parameter values		
Mode	Frequency $\omega_{s,a}$ [GHz]	Magic power [dBm]
ASM	5.46	-35
SM	5.97	-31.5

Because these mode frequencies depend on the bare frequencies of the qubits which in turn depend on the applied magnetic flux, the SM could be studied for different configurations of the applied fluxes in both flux lines. By fixing the input voltage to one of the flux lines, while sweeping the input voltage of the other over $V_i = [-2, 2]$ V and recording the trace (S_{11} in the VNA, centered at ω_s), the change in the mode frequency could be observed. This was done at the magic power of the SM and a total of four sweeps were performed, differing from each other by the choice of the fixed voltage values. These fixed applied voltages for the flux generating elements 1 and 2 were arbitrarily chosen to be $V_1 = 0, 1.6$ and $V_2 = 0, 2$ V. For each iteration of the sweeps the SM resonance frequency could be extracted from the dips and giving us four data sets shown in Figure 3.5. These data sets could then be used to fit the parameters in our model (using equation 3.2 and the *curve_fit* function in the python scipy library) resulting in an estimate of the inductance matrix. The obtained environmental offsets were $\phi_{e1}/\phi_0 \approx -0.0004$ and $\phi_{e2}/\phi_0 \approx 0.0062$ and the

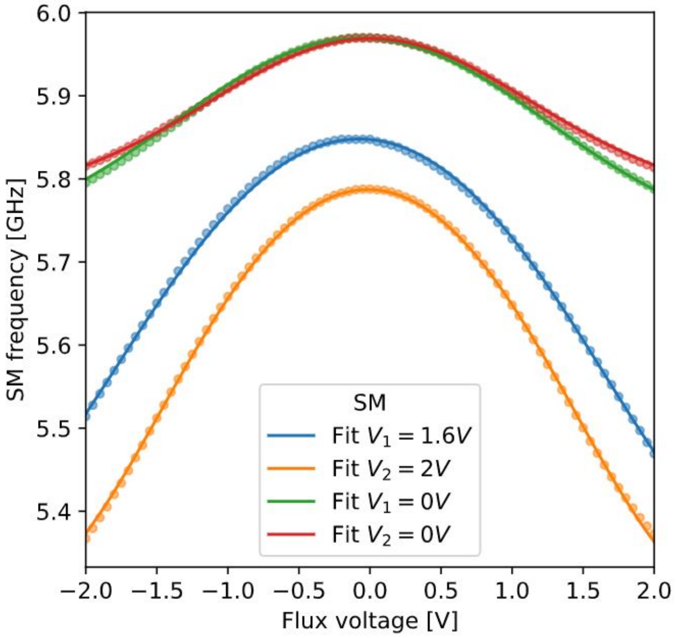

Figure 3.5: Flux dependence of the SM resonance frequency ω_s. Four different data sets were taken while sweeping one of the applied fluxes and keeping the other fixed. The data was then fitted with our model of the dressed qubit frequencies using equation 3.2.

elements of the obtained inductance matrix are shown in Table 3.2. By inverting the inductance matrix in our flux model 3.1, it was then possible to know what voltages to apply in order to apply a certain magnetic flux to the qubits. Additionally we note that the cross coupling consisting of the M_{12} and M_{21} are very small.

Table 3.2: Obtained matrix elements of the inductance matrix.

$M_{ij}/\Phi_0\,[V^{-1}]$	$i1$	$i2$
$1j$	0.1086	0.0009
$2j$	0.0003	0.0935

Having a way to find out how much flux is applied due to a given voltage the next step was to determine which flux configuration corresponded to a fully hybridized state. To this end the flux voltage for flux line 1 was fixed at $V_1 = 1.6\text{V} \longrightarrow \phi_2/\phi_0 \approx 0.18$. Next the applied flux of the other flux line was sweeped from 0 to 3 V while both the SM and ASM frequencies were monitored through their respective waveguides. The point at which the difference between the two mode frequencies was the smallest i.e. $\omega_s - \omega_a = 2g$, was found at $V_2 = 2.07\text{V} \longrightarrow \phi_2/\phi_0 \approx 0.2$ as seen in Figure 3.6.

With the newly applied flux, the new mode frequencies and their separation corresponding $2g$ are presented in table 3.3 along with the initial values. With these new values of SM and ASM the next step was therefore to calibrate the TWPA in the ASWG to yield the best possible gain with the least amount of noise.

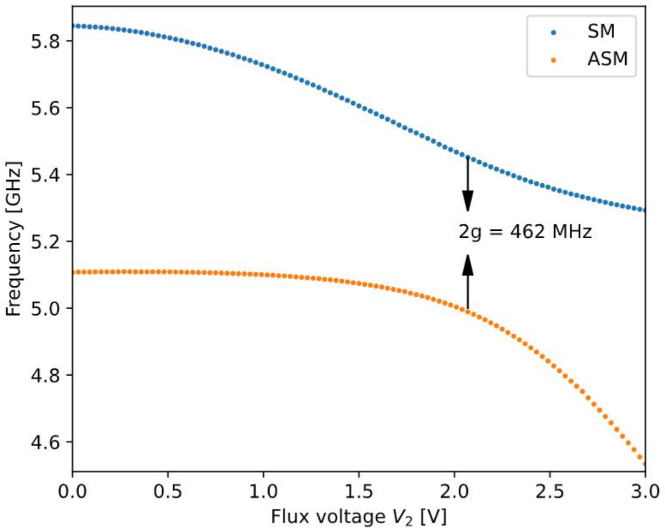

Figure 3.6: Resonance frequencies of both ω_s and ω_a observed through their respective waveguides. The applied voltage to flux line 1 was fixed at $V_1 = 1.6$ while sweeping V_2. The point at which the difference between the mode frequencies are the smallest corresponds to $2g$ and represents a fully hybridized state (equal bare qubit frequencies).

Table 3.3: Characterization parameters divided with 2π with applied flux ϕ/ϕ_0.

Parameter values		
Parameter [GHz]	$\phi_1/\phi_0 = 0$ $\phi_2/\phi_0 = 0$	$\phi_1/\phi_0 \approx 0.18$ $\phi_2/\phi_0 \approx 0.20$
ω_a	5.46	4.99
ω_s	5.97	5.45
$2g$	0.50	0.46

3.2.2 TWPA calibration

As previously mentioned the TWPA requires both a pump tone along with a DC bias given by applying a voltage into its flux line. The aim was therefore to find the pump and flux configuration yielding the best gain while also adding the least amount of noise. To this end the method presented by Slawomir *et al.* [50] was followed and included the usage of a spectrum analyzer (SA) to measure the power spectrum in units of dBm/Hz.

The measured spectral density when using a SA is obtained as P_{out}/B where B is the resolution bandwidth in the context of the spectrum analyzer. The measured power spectra resulting from e.g. the thermal noise photons with temperature T_{in} right in front of the ASWG then depend on the gain and attenuation of the output line. As seen in the wiring diagram in Figure 3.4, the line coming from the ASWG includes two amplifiers, namely a TWPA and a HEMT. These both contributes by amplifying the signal but with some added noise corresponding to the temperatures

T_{TWPA} and T_{HEMT}. If we disregard the noise photons added by the rest of the line (assumed to be very small), the measured power spectral density can be expressed as [50]

$$\frac{P_{out}}{B} = G_{tot} k_B \left[T_{in} + T_{TWPA} + \frac{T_{HEMT}}{G_{TWPA}} \right] \tag{3.4}$$

where G_{TWPA} is the gain from the TWPA and G_{tot} the total gain of the output line. If the input noise temperature is a experimentally controllable parameter, this equation is linear function of T_{in}.

In order to control the input noise temperature, an arbitrary waveform generator (AWG) was used. This is a very useful instrument which can output arbitrary waveshapes specified by the user. The output is usually defined from an array containing specific voltage targets that are to be met at specific times along the waveform. An AWG can then jump between these targets or interpolate between them. Therefore the usage of a AWG is perfectly suited for generating white noise. This was done with a previously developed Labber driver which generates random points with some user defined amplitude. Taking the Fourier transform and then filtering (square filter) it to only include frequencies over some specified bandwidth, an inverse Fourier transform could then be performed resulting in an array of values voltage targets that could be sent to the AWG. The result when looking at this engineered noise in a SA is then a square of white noise over the specified bandwidth. The input noise temperature T_{in} is then proportional to the amplitude of the white noise and can therefore be viewed as a *heat bath*. However, the point of interest regarding the TWPA performance was at the frequency $\omega_a = 4.99$ GHz around which the noise had to be centered. Because the AWG used (Keysight M3202A) was limited to 1 GSa/s, the noise had to be upconverted using a local oscillator (generating a continuous sinusoidal tone at some specified frequency) and a mixer as depicted in Figure 3.7. The output signal from the mixer then contains the frequency of the LO ± the frequency sent in by the AWG. By centering the noise frequency at 100 MHz with a bandwidth of 40 MHz and setting the LO frequency at 5.09 GHz, the signal going into the input line towards the AWG contained two heat baths (white noise) centered around 4.99 GHz and 5.19 GHz. Because the frequency point of interest was around 4.99 GHz, the other side-band at 5.19 GHz was neglected along with any affects it could have on the TWPA performance.

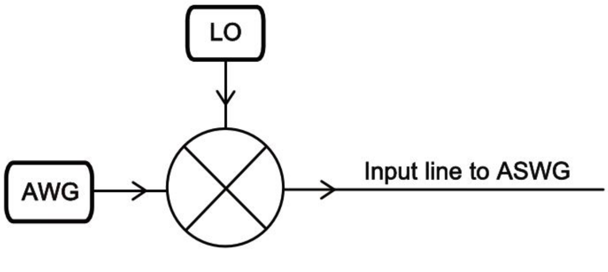

Figure 3.7: Upconversion of the output from the AWG using a LO and a mixer. The output is sent into the input line towards the ASWG.

Using this heat bath setup the input noise temperature T_{in} could thus be controlled by varying the amplitude of the noise. From equation 3.4 we note that the slope of this linear function corresponds to the total gain of the output line. This equation can also be reformulated as $T_{in} = \alpha P_{out} - T_{added}$ where T_{added} correspond to the added noise photons from the amplification chain. Therefore we can interpret the point at which the function intersects with the x-axis (total noise of the system) as the added noise. In order to investigate how the added noise and gain was affected by different TWPA parameters, the following measurement was performed: The TWPA pump power was set to 10 dBm at 9 GHz which was chosen to be around double that of the signal coming into the TWPA in accordance with recommendations from the company VTT who made it. The TWPA flux was also initially set to 2.3 V. Monitoring a single point at frequency 4.99 GHz using the spectrum analyzer with a resolution bandwidth of 50 kHz, the input noise amplitude was swept from 0.2-0.8 V in six steps. At each step a total of 350 averages was collected. These six data points were then collected while sweeping both the TWPA flux up to 2.7 V (in 26 steps) and the TWPA pump frequency up to 11 GHz (in 26 steps). By performing a linear fit on all these data sets (each containing six points) and extracting the slope and intersection points of these fits, the plots in Figure 3.8 could be constructed. From these plot we clearly see the effect of the usage of different TWPA parameters.

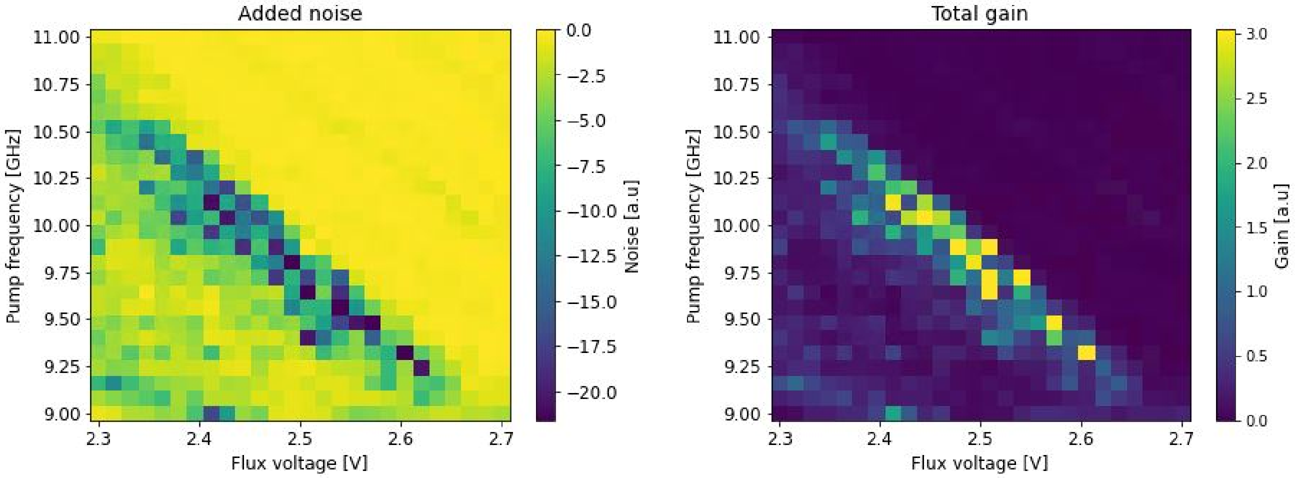

Added noise

Total gain

Figure 3.8: The added noise and total gain obtained from the linear fits of the acquired data when sweeping the input noise amplitude at different TWPA flux voltages and pump frequencies. Note that the points with the least added noise coincides with the largest gains.

The low noise regions correspond to high gain regions as expected since a line with a steep slope will intersect earlier than a line with a small slope. These plots therefore gave an indication to what parameter combination would yield good results and the choice was made to use a TWPA flux voltage of 2.46 V and TWPA pump at 10 dBm and 9.7 GHz. The pump frequency was later slightly changed when investigating the symmetry of the Mollow triplet (which will be discussed later) resulting in 9.72 GHz. The reason behind this additional calibration was due to the spectral gain profile of the TWPA not being flat, resulting in a noticeable gain differences over a narrow frequency span. Through measurements with the VNA around the ASM frequency, it also turned out that this combination of parameters yielded a total gain of around 17 dB compared to when the TWPA was off (no pump or flux).

3.2.3 Coupling rates

When studying the reflection in a waveguide as described in section 2.3.1, the measured scattering parameter S_{11} depend on the power of the coherent tone sent into the waveguide. We recall that the power enters the theoretical expression for the reflection (equation 2.47) along with the different coupling rates Γ_r, Γ_{nr} and Γ_ϕ. However the actual power at the end of any of the waveguides depend both on the input power but also on the actual attenuation along the input lines. Therefore we can express the driving rate as

$$\Omega = 2\sqrt{\frac{\Gamma A P_{out}}{\hbar\omega}}. \tag{3.5}$$

where A corresponds to the attenuation and P is the output power in Watts from the VNA. By sweeping the output power P_{out} and recording the scattering parameter S_{11} in the VNA around the SM (from the SWG) and then the ASM (from the ASWG), data sets similar to what is shown in Figure 2.6 were acquired. These data sets could then be fitted by using the modified expression for the driving rate Ω in the theoretical expression for the reflection. The fitting was done in python and utilized the least squares function in scipy. By doing so, the total attenuation along with all the coupling rates were found. However, because it is hard to distinguish between the pure dephasing rate Γ_ϕ and the non-radiative dephasing rate Γ_{nr} (they behave similarly in the reflection expression), the pure dephasing rate was set to zero and thus omitted in the fitting.

The next step was to determine how applied noise into one of the flux lines affected the pure dephasing rate. To this end, the noise sent into flux line 1, was constructed in a similar manner to how the noise was generated when calibrating the TWPA. It does however turn out that the noise has the greatest effect when centered around the difference in mode frequency, which we previously found to be equal to $2g = 462$ MHz. However, greater care was here taken in order to have completely white noise by utilizing both LP-filters, DC-blocks and an extra amplifier. The circuit going into the flux line is illustrated in Figure 3.9. The LO was fixed to 820 MHz resulting in that the up-converted center frequency of the noise could be adjusted. The bandwidth of the noise was chosen to be 40 MHz and by choosing the center frequency to be 358 MHz, the up-converted noise would be centered at $2g$. The spectral shape of the noise used in this obtained using a SA is shown in Figure 3.10 along with a off-centered example. In order to get a relationship between the amplitude of the applied noise and the pure dephasing rate, the reflection around the SM was measured at the SM magic power. By varying the noise amplitude while monitoring the reflection the obtained data could be fitted using the previously found coupling rates and only using the pure dephasing rate as the fitting parameter.

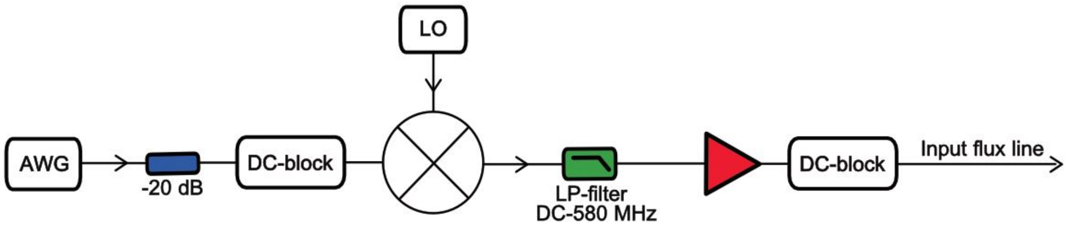

Figure 3.9: Circuit for applying dephasing noise going into flux line 1. DC-blocks, filter and attenuator were added in order to prevent reflection and unwanted frequencies passing through.

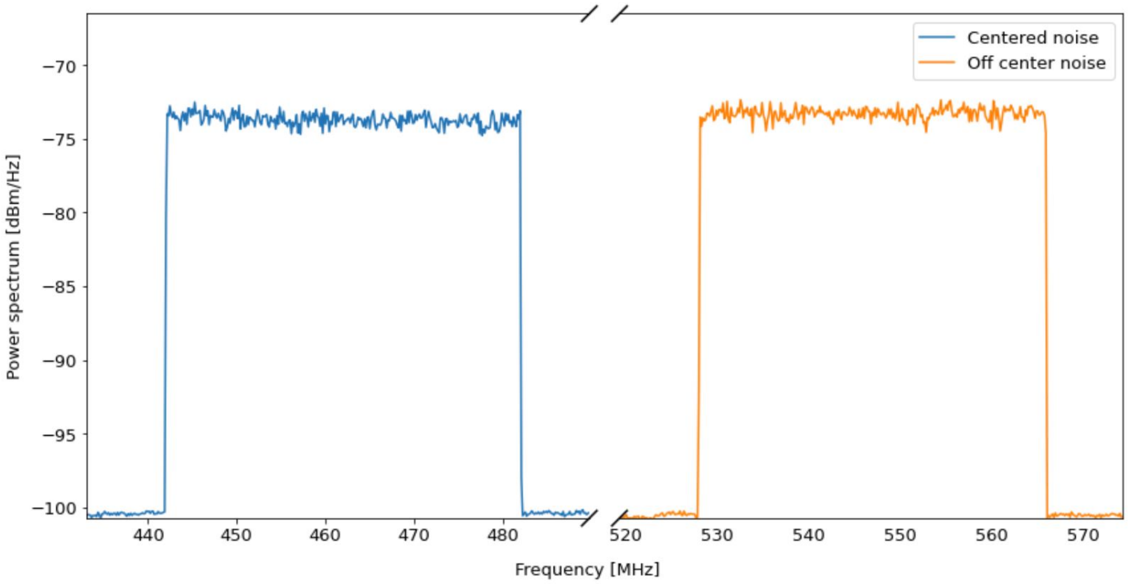

Figure 3.10: The shape of the dephasing noise sent into flux line 1 (centered noise) when looked at with the SA. In contrast to the (blue) spectrum which is centered around $2g$, this plot also illustrates a off centered example (orange).

3.3 PSD measurements

The purpose behind the main experiments for this thesis was to measure heat flows. These experiments relied heavily on an in-house developed Labber driver allowing the user to setup and define pulse sequences to be outputted by an AWG and then recorded by a digitizer (DIG). The driver utilized the power of a field programmable gate array (FPGA), enabling the user to sweep several pulse defining parameters (e.g. amplitude) in real time without having to upload new configuration files to the AWG. The parameters of a pulse could thus be swept over a number of iterations which could then be repeated over a certain number of averages. In other words, for each iteration, a pulse parameter was changed. The digitizer then separately recorded each iteration resulting in a large number of traces (the number of averages times the number of iterations) which could then be averaged in an interleaved fashion. In this thesis two iterations were used between which the amplitude of an

11 μs pulse with no carrier frequency (square pulse) was swept between 0 and 1 V with $2 \cdot 10^4$ averages. This meant that the pulse with amplitude 0 V was first outputted by the AWG followed by the 1 V, which was then again followed by the 0 V pulse etc... The interleaved averaging over these iterations could then be performed in software on the data acquired by the DIG. However, before performing the interleaved averaging, the PSD of the obtained time traces calculated as the modulus squared of the signals Fourier transform using the python library scipy.

The role of this setup will become apparent in the following sections when we describe how the Mollow triplet was used both for calibration purposes and observing excitation transfers. After the Mollow triplet experiments had been performed the heat bath experiments were finally done with the goal of measuring heat flows.

3.3.1 Calibration with Mollow triplets

Apart from the previously discussed circuit used for dephasing, the room temperature circuits used for all PSD measurements also included the circuit going to the input line, Figure 3.11 (a) and the one coming from the output, Figure 3.11 (b). These circuits were used for the input/output for both the SWG and ASWG. The mixers used were IQ mixers which for the up-conversion [Figure 3.11 (a)] could be calibrated to only send out the left side band as the RF signal (RF then corresponded to the LO frequency minus the IF frequency). Furthermore the LO used for the up-conversion was gated by AWG1 so that for a pulse above a certain threshold value, the LO would emit a RF tone and otherwise not. This AWG1 was in turn controlled using the previously described Labber driver. The purpose behind this was that the LO would then only output a signal during the time it received a nonzero signal from the AWG. By iterating the amplitude of the pulse outputted by AWG1 as previously described, the LO would therefore effectively turn on and off at an interval of 11 μs determined by the pulse duration coming from the AWG. The signal to be up-converted was in turn set with another Labber driver, controlling a second AWG termed AWG2 in the Figure below. However, because the sampling rate of the digitizer used (Keysight M3102) was 500 MSa/s the signal coming from the output line had to be down-converted as shown in Figure 3.11 (b). Since the DIG was also controlled through the same Labber driver as the AWG, the recorded data was obtained as previously described including both PSD calculations and interleaved averaging.

In order to measure the Mollow triplet in each of the SM and ASM, the AWG2 used in the up-conversion was set to output a sinusoidal tone at 100 MHz while the frequency for the two LOs (one for each input line) was set to be $\omega_{\{s,a\}}$+ 100 MHz. The amplitude of the tones generated by AWG2, would then determine the driving rate Ω for the two TLS corresponding to the SM and ASM and was therefore set to be 150 mV and 30 mV respectively (values determined through trial and error). Because, for example, iteration 1 did not send pulse, the LO was not activated resulting in that the PSD of the output only contained background noise. In iteration 2 however, a pulse was sent to the gate of the LO which then activated, resulting in

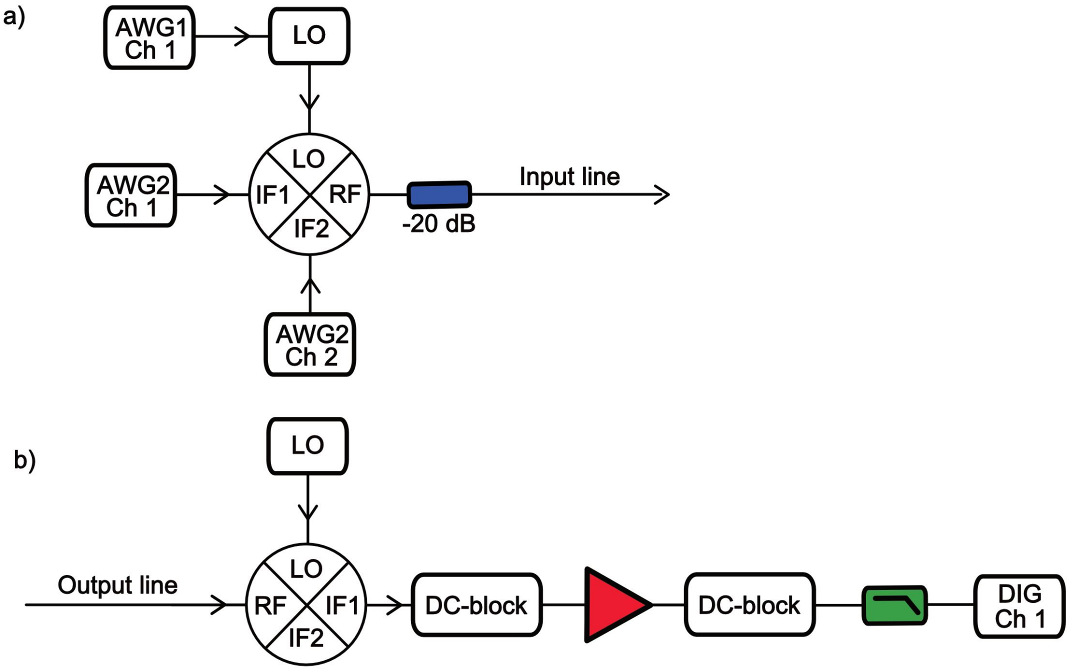

Figure 3.11: a) Upconversion of the signal coming from AWG2. An IQ mixer was used to only send in the left side band coming (RF corresponded to the LO frequency minus the IF frequency). The LO was also turned off and on by sending in square pulses from AWG1 with amplitudes set to 0 and then 1 V at 11 μs intervals. b) Down-conversion and amplification of the signal going into the digitizer. The PSD of the obtained traces were calculated followed by interleaved averaging.

a recorded output that contained the Mollow triplet on top of the background noise. Using both of these traces, the background could be subtracted from the trace containing the Mollow triplet resulting in a trace where the PSD was zero everywhere except around the Mollow triplet.

Because the interleaved averaging was done in software and due to memory limitations, only $2 \cdot 10^4$ averages per measurement could be taken. By repeating the measurement a total of $5 \cdot 10^6$ averages were obtained for the ASM Mollow triplet and $8 \cdot 10^6$ averages for the SM Mollow triplet. The reason for the smaller number of averages taken for the ASM triplet was the increased SNR on that line due to the TWPA.

The obtained PSD did not however, correspond to the PSD that would have been found right in front of the device inside of the waveguides. This was due to the amplification chain between the device and the DIG. The PSD in the waveguide was desired because the photon number can effectively be calculated by dividing the PSD with the photon energy $\hbar\omega$, as we know that this relates to the temperature. In order to obtain the photon number we turned to the theoretical expression for the Mollow triplet (equation 2.50) and it turns out that its integral divided by the photon energy gives the total photon flux as

$$\int_{-\infty}^{\infty} \frac{S(\omega)}{\hbar\omega_0}\, d\omega = \frac{\Gamma_r}{2}. \tag{3.6}$$

Note the assumption that the difference in photon energy between the centre frequency ω_0 and the other surrounding frequencies is small. From previous measurements the radiative coupling rates Γ_r for both the SM and ASM were known. Therefore the area obtained Mollow triplets could be normalized to $\frac{\Gamma_r}{2}$ and by dividing by $\hbar\omega_0$, the scaling factor relating the obtained PSD to the actual photon number could be obtained. These two scaling factors were then used in all subsequent PSD measurements to calibrate the y-axis of the obtained PSD plots to correspond to the number of photons.

3.3.2 Excitation transfer

In order to observe excitation transfer between the SM and ASM due dephasing induced by applying noise, Mollow triplets could be used. Instead of exciting both the SM and ASM, only the SM was excited by setting the amplitude for the up-converted signal going to the ASWG to zero and the amplitude going to the SWG to 30 mV. The reason for the decreased amplitude going into the SWG was to only observe the centre peak of the triplet (the driving rate was too small to result in visible side bands). By simultaneously recording data for both Mollow triplets while sweeping the dephasing noise amplitude as described in section 3.2.3 (using a third AWG), excitation transfer could be observed. However, because a large number of averages was required to obtain data with low SNR, the noise amplitudes were only being sweeped four different values corresponding to 0, 67, 133 and 200 mV.

3.3.3 Heat baths

The main experiments consisted of sending in heat baths into the SWG and ASWG and observing the heat flow as a function of noise induced dephasing. The circuits used were the same as for the Mollow triplet measurement with the difference that the up-converted signal no longer consisted of a sinusoidal tone but instead of white noise acting as a heat bath (constructed in the same way as the heat bath in the TWPA calibration). The bandwidth of these two heat baths were 20 MHz centered at the SM and ASM frequencies respectively with a spectral profile $S(\omega)$ as shown in Figure 3.12.

The main principle behind the experimental setup is shown in Figure 3.13 where the SWG has a higher temperature than the ASWG. These temperatures are determined by amplitudes of the aforementioned heat baths that are sent into the input lines. The noise induced dephasing then results in excitation transfer and thus changing the populations as discussed in section 4.8 and 1.3. This then results in a competition between separate thermalization of the two qubits with their corresponding heat bath and population equilibration due to the dephasing. In the case depicted in Figure 3.13, the SM will absorb photons from the SWG while the ASM emits photons into the ASWG. The decrease and increase of photons in the respective waveguides can then be observed as a dip at ω_s and peak at ω_a when measuring the PSD. A dip then correspond to a negative photon flux while a peak reflects a positive photon flux. This example therefore illustrates the expected behaviour of our system operating as a heat engine where photons (heat) flows from the hot to the cold thermal bath.

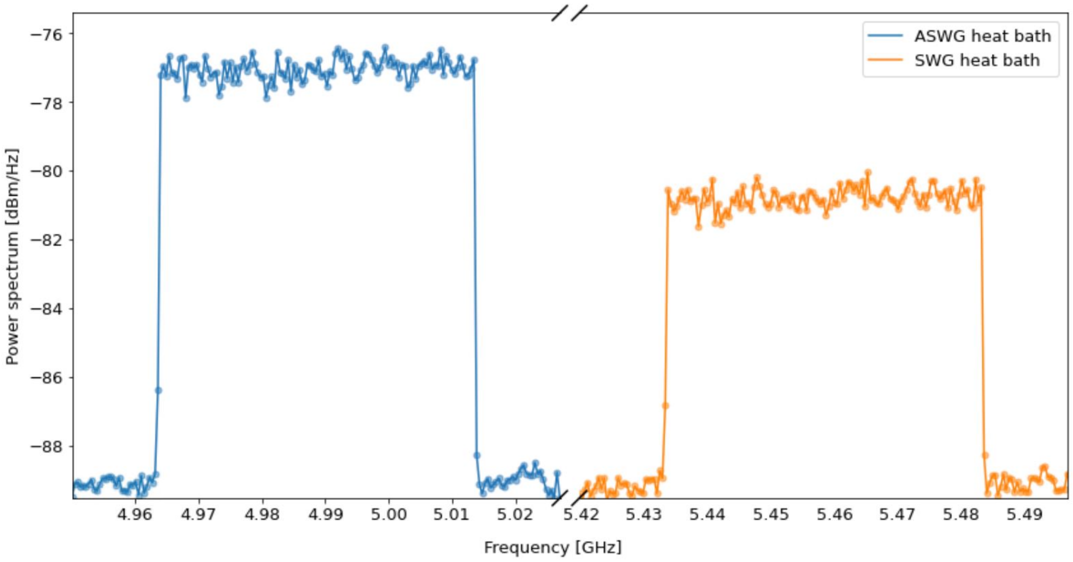

Figure 3.12: Power spectrum of the heat baths sent into the two waveguides. Note that the amplitudes here are not the same as those actually sent into the waveguides.

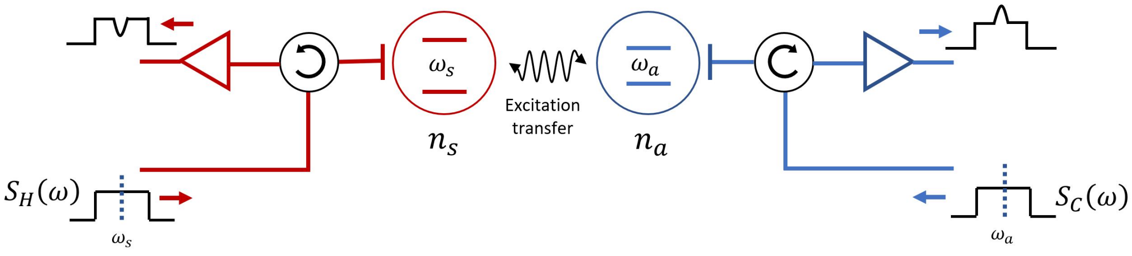

Figure 3.13: Working principle behind the experimental setup when the device operates as a heat engine. When measuring the PSD of the hot heat bath coming from the SWG a dip at ω_s can be seen. Similarly a peak will be observed at ω_a when measuring the PSD from the output of the ASWG.

4

Results

In this chapter the main results from the measurements are presented in two parts. To begin with the results from characterization of the system and the effects of noise induced pure dephasing obtained through spectroscopy are given. The second part then presents the findings from the different PSD experiments involving Mollow triplets and heat baths.

4.1 Spectroscopy

After the the desired flux points had been found along with the relationship between the applied flux voltage and actual magnetic flux Φ, the coupling rates were obtained through spectroscopy as described in section 3.2.3. The S_{11} data used for modeling the theoretical expression for the reflection in the SWG is shown in Figure 4.1. As expected from theory the reflection goes to zero around the magic power due to coherent scattering at the TLS resulting in complete destructive interference. In addition to the dip in reflection when looking at $|S_{11}|$, the expected phase flip is also present. From a similar dataset taken from the ASWG the new magic powers

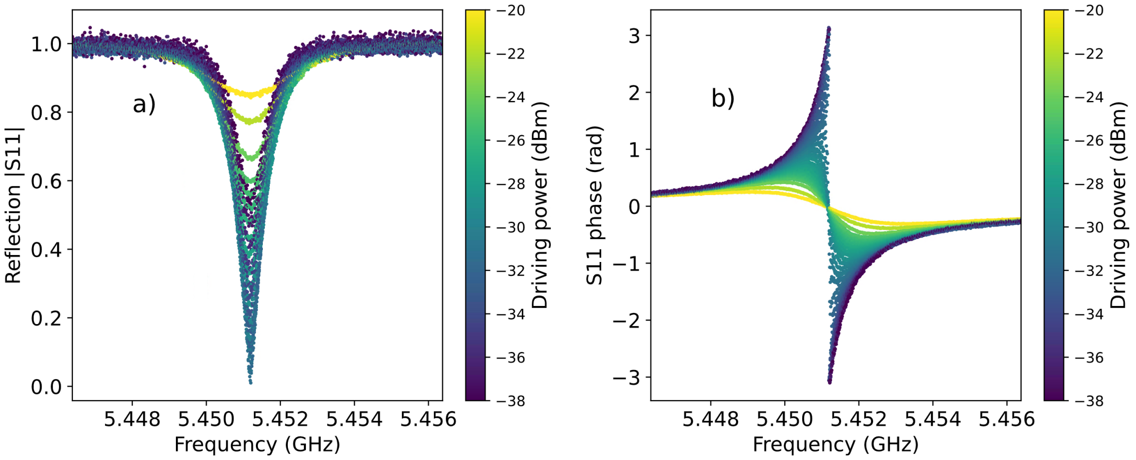

Figure 4.1: Obtained data of the scattering parameter S_{11} from the SWG for several different input (driving) powers. a) Reflection $|S_{11}|$ showing a clear lorentzian dip around the mode frequency with the largest dip at the magic power. b) A complete phase flip of π rad occurs at the magic power where the coherent scattering results in complete destructive interference.

(when applying magnetic flux) were found to be -31.5 and -37 dBm for the SM and ASM respectively with the coherent drive rates $\Omega_{\{s,a\}} \approx \frac{\Gamma_{\{s,a\}}}{\sqrt{2}}$. In addition to the data gathered with applied fluxes, the same data was taken without any applied flux resulting in a total of four data sets. While keeping the pure dephasing rate fixed at zero, the radiative $\Gamma_{\{s,a\}}$ and non-radiative $\Gamma_{\{s,a\},nr}$, the coupling rates were fond by modeling the data using equation 2.47, yielding the rates shown in table 4.1. The non-radiative losses to the environment were as expected much smaller compared to the radiative coupling rates to the waveguides.

Table 4.1: Radiative and non-radiative coupling rates with and without applied flux Φ/Φ_0. The numerical values have been divided by 2π in order to get them in units of Hz.

Parameter values		
Parameter [MHz]	$\Phi_1/\Phi_0 = 0$ $\Phi_2/\Phi_0 = 0$	$\Phi_1/\Phi_0 \approx 0.18$ $\Phi_2/\Phi_0 \approx 0.20$
Γ_s	0.86	1.21
$\Gamma_{s,nr}$	0.04	0.07
Γ_a	0.58	0.57
$\Gamma_{a,nr}$	0.02	0.05

One additional coupling-rate which has not been accounted for and assumed negligible in this study is the potential cross-coupling rate between e.g. the ASM and the SWG. Apart from cross-talk between RF lines, spurious capacitive couplings on the chip, one of the biggest contribution to this cross-coupling rate is imperfect hybridization. The explanation to why this coupling rate was disregarded lies in that its effects are seen as leakage, such as scattered radiation from the ASM going into SWG. This leakage depend on how equal the two bare qubit frequencies are to each other i.e. if the qubits are fully hybridized or not. When they are not fully hybridized one cannot say that the SM and ASM have well defined parities (not fully symmetric and antisymmetric), which leads to the cross-coupling. This could be seen when measuring the reflection from the SWG while fixing the applied flux in flux line 1 to $\Phi_1/\Phi_0 \approx 0.18$ and sweeping the flux of flux line 2. The measured reflection in this case case is shown in Figure 4.2, where there is a noticeable leakage from the ASM which gradually disappears as the qubits become more hybridized. As previously discussed the flux voltage of flux line 2 was chosen as to where the difference of two dressed frequencies were smallest since this corresponded to a fully hybridized state with equal bare frequencies and thus minimal leakage. This is therefore the reason why the cross-coupling rate was neglected.

The final coupling rate to be determined was the pure dephasing rate and how this depended on the applied noise power through one of the flux lines. By fixing the input power to the magic power and sweeping the amplitude of the centered input noise (shown in Figure 3.10) this dependence could be determined by fitting the data and only using the pure dephasing rate as a fitting parameter. The result of the fits as shown in Figure 4.4 were very good and gave a linear relationship between the applied dephasing power V^2 and the pure dephasing rate. By doing a linear fit on these data points one can model the dephasing rate as $\Gamma_{\phi,s} \approx 16.674V^2 + 0.006$ giving us a way of mapping noise power to a desired dephasing rate. We also note that at zero noise power we do have some inherent dephasing present in the system. However, the fits of the data obtained from the ASWG were not as good and as the one from the SWG and could thus not be used as a reliable way of mapping the dephasing rate to the noise power. Even though the fit from the ASM was not perfect, it yielded a linear relationship quite similar to that of the SM as seen in Figure 4.3. Because the noise only affects one of the qubits but the SM and ASM both depend on that qubit, it should not matter in which flux line the noise is applied and the dephasing rates were expected to be equal $\Gamma_{\phi,a} \approx \Gamma_{\phi,s}$. The obtained fits are however quite similar and due to the poor fit from the ASM we can assume that the dephasing rates are approximately equal allowing us to use the model for $\Gamma_{\phi,s}$ to map the dephasing to the applied noise power.

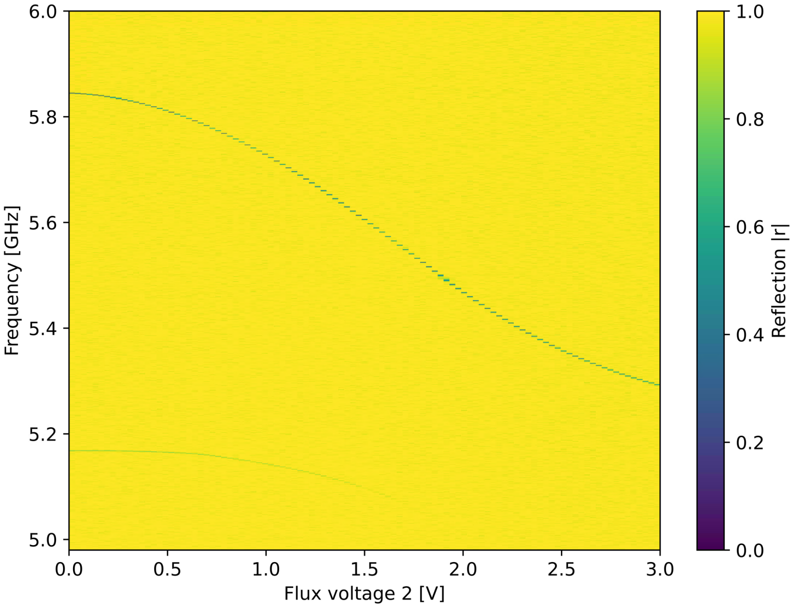

Figure 4.2: Measured reflection $|r|$ from the SWG while sweeping the the applied voltage of flux line 2 and keeping the other flux fixed at $\Phi_1/\Phi_0 \approx 0.18$. The scattering from the ASM can be seen leaking into the SWG but gradually disappears when the qubits become more hybridized at higher flux voltages.

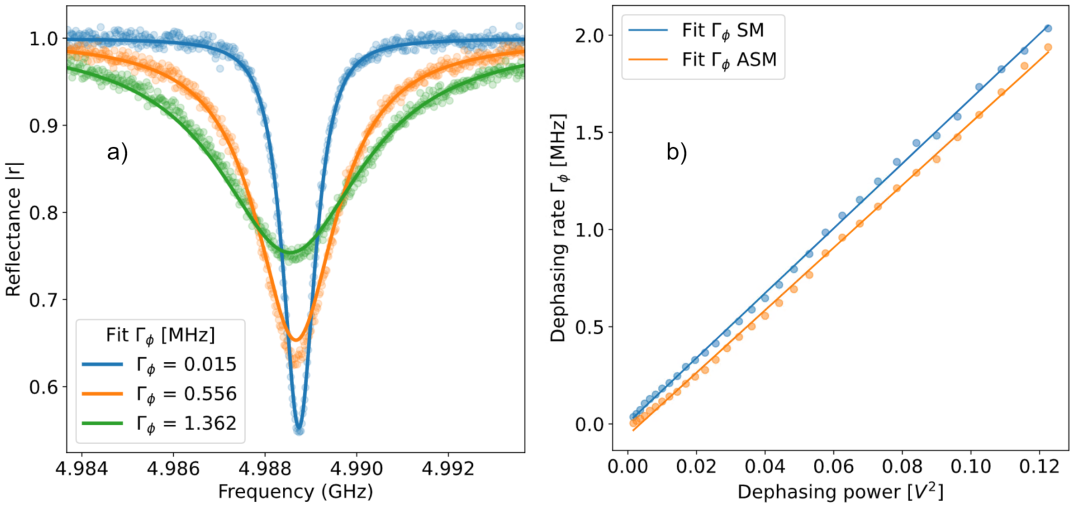

Figure 4.3: a) Reflection fit for ASM when sweeping the dephasing power using the theoretical model in equation 2.47 where the pure dephasing rate was kept as a variable parameter while the rest were fixed to their previously obtained values (from table 4.1). The figure shows the fits for a few powers and as indicated by e.g. the orange line, the fits were not as good as the ones obtained for the SM, as shown in Figure 4.4. b) Linear fits of the pure dephasing rate obtained as a function of noise power V^2 for both the SM and ASM. The reason why the linear fits are not the same is most likely due to the poor fit from the ASM as seen from the orange fit in figure (a).

4.2 Mollow triplet and Excitation transfer

The Mollow triplets from both the SM and ASM are shown in Figure 4.5. From the theory behind the Mollow triplet, we know that the frequency difference between the centre and side peaks corresponds to the driving rate. Using the theoretical model of the triplet (equation 2.50) and fitting it to the data, it was possible to determine that the 150 mV amplitude going into the SWG corresponds to $\Omega_s \approx 5.4$ MHz and the 30 mV going into the ASWG resulted in a driving rate of $\Omega_a \approx 3.4$ MHz. We also note that that in the case of applied dephasing, the driving rate is reduced by around 0.4 MHz for both the SM and ASM. When looking at the expression for the driving rate Ω in equation 3.5, the only parameter that could have changed is the coupling rate to the waveguide. One can therefore conclude that with increased dephasing follows a slight decrease in the coupling rate (in this case about 0.16 MHz). This can be explained from the fact that the coupling rate depend on the mode frequency, and as seen in Figure 4.3, the mode frequency do shift slightly at higher noise powers. The gradual disappearance of the dip seen in Figure 4.4 could therefore have a twofold explanation. One is that the dephasing results in incoherent scattering and the other is a gradual reduction in the radiative coupling rate. It would therefore be interesting in further studies to explore the Mollow triplet in even higher dephasing regimes.

The normalization of the gathered data in regards to the theoretical value of the

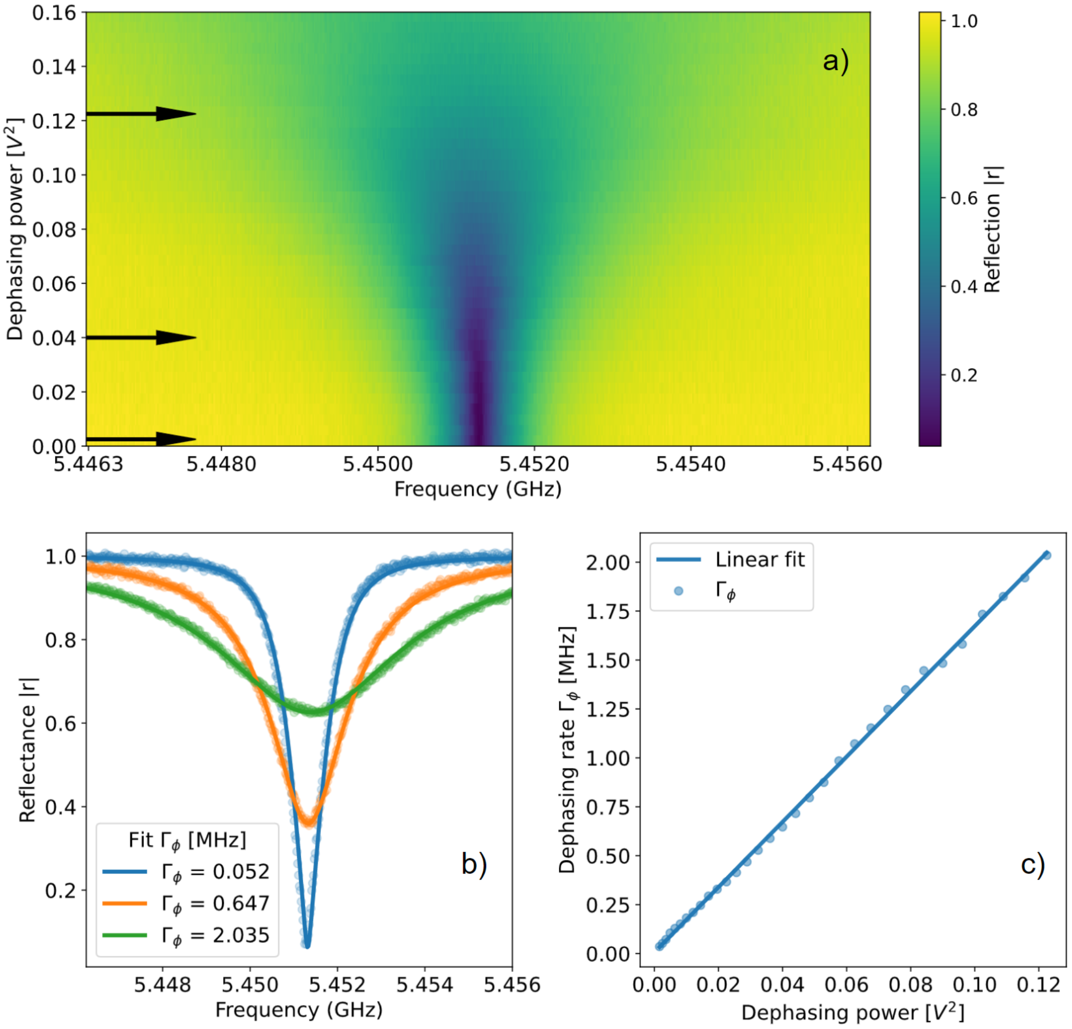

Figure 4.4: a) Measured reflectance from the SWG with input power fixed at the magic power of the SM while sweeping the amplitude of the applied noise. b) The arrows in a) indicate the displayed line cuts marked as dots in the figure. The lines indicate the theoretical model obtained using equation 2.47 where the pure dephasing rate was kept as a variable parameter while the rest were fixed to their previously obtained values (from table 4.1). c) The pure dephasing rates found from the fits shows a linear relationship to the dephasing power V^2.

photon flux (area under the data) being equal to $\frac{\Gamma_{\{s,a\}}}{2}$, yielded the scaling factors $G_a = 3$ and $G_s = 55.8$ which in combination with the photon energies $\hbar\omega_a$ and $\hbar\omega_s$ could be used to get the photon number on the y-axis. These scaling factors could also be used in order to estimate the number of thermal photons in the waveguide plus the number of added photons due to the amplification chain in each output line. Because every other iteration in the measurement of the Mollow triplet only contained the background noise, these “noise photons“ could be found as the non-scaled difference between one of the side peaks of the triplet and the background noise level at that frequency. Using the scaling factors the estimated number of noise photons were found to be $N_{a,noise} = 5.27 \pm 0.05$ for the ASWG and $N_{s,noise} = 18.77 \pm 0.17$ for the SWG. This is a clear indication of how the TWPA greatly reduces the number of added noise photons. The reason the TWPA do not result in noise photons closer to 1 photon (0.5 photons from vacuum fluctuations at the input and 0.5 photons from minimum added noise) is probably because of the calibration not being perfect, some thermal background and a finite attenuation between the sample output and TWPA input.

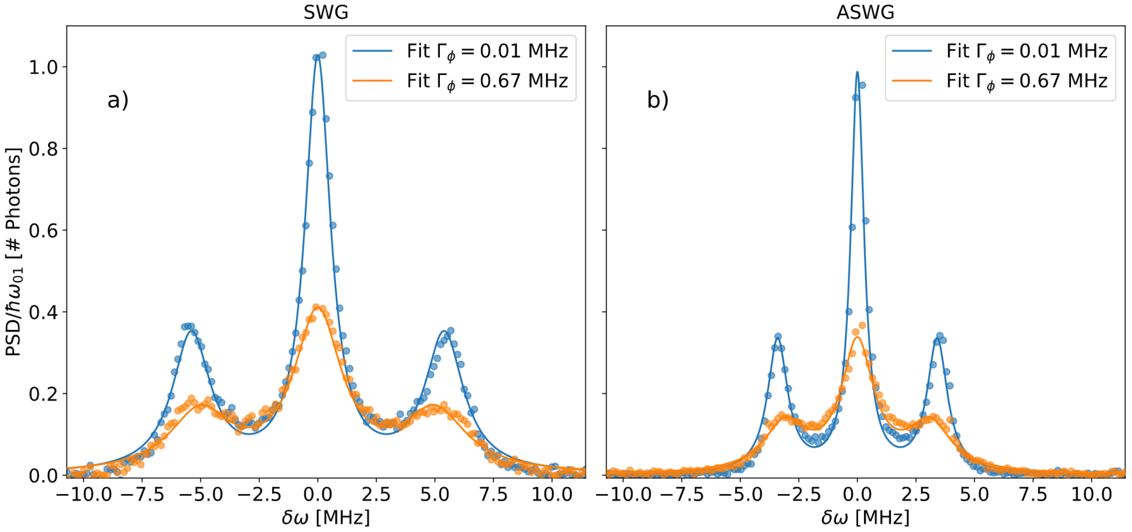

Figure 4.5: a) Mollow triplet from the SWG with and without applied dephasing noise. Dots indicate the measured data while the lines corresponds to the theoretical model of the triplet obtained using equation 2.50. All parameters in the theoretical expression were set to variable parameters except the mode frequency. b) Mollow triplet from the ASWG also with and without added dephasing. As expected the triplet from the ASWG is smaller then the one from the SWG due to the lower coupling rate.

The observation that the SWG Mollow triplet is much bigger (larger area under the curve) than the ASWG triplet, helps mitigating the previous concern that the value of the radiative coupling rate $\Gamma_s = 1.21$ MHz is a local but not global minimum. Additionally the dephasing results in a reduction in the photon flux of about 31% in the SWG and around 25% in the ASWG. Because the Mollow triplet measurements for the two modes were done separately, one can explain these reduced photon fluxes to be a result of excitation transfer. However the reason of them not being equal might stem from a wrongful assumption that $\Gamma_{\phi,a} \approx \Gamma_{\phi,s}$ and that the difference in the linear fits in Figure 4.3 is not only due to poor fitting but also an inherent property of the system.

In order to study the excitation transfer more explicitly only the SM was excited but with a lower driving rate resulting in that only the center peak was visible. By monitoring both output lines while increasing the dephasing, clear excitation transfers were observed as seen in Figure 4.6. With no applied dephasing a peak is only seen in the SWG but when increasing the noise amplitude and thus the dephasing rate, a peak also starts to appear in the ASWG. When fitting Lorentzian functions to these peaks and numerically integrating the fitted functions, the total photon flux ϕ_{photons} into both of the waveguides could be calculated. It also becomes apparent that the total flux slowly decreases until $\Gamma_\Phi = 0.67$ MHz. The reason for the decrease is most likely due to the reduced coupling rates to the waveguides as a consequence of the increased dephasing rate.

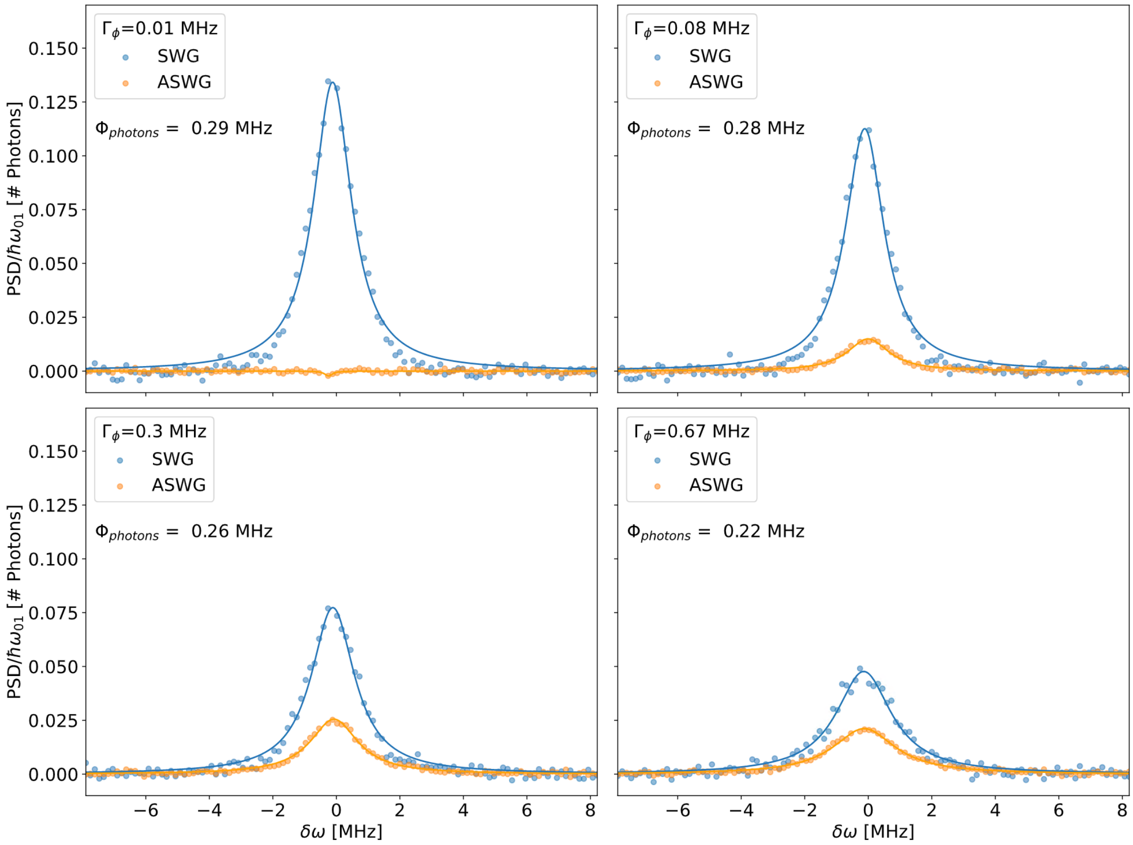

Figure 4.6: Excitation transfer seen by exciting through the SWG and observing the Mollow triplet (only centre peak due to low driving rate) in both waveguides. Dots indicate the measured data while the lines corresponds to lorentzian fits where the amplitude, width and center were used as variable parameters. When increasing the dephasing rate a peak appears in the ASWG even if we are not actively exciting the ASM through its waveguide. The total photon flux into both waveguides slowly decreases with increased dephasing, probably due to the decreased radiative coupling rate.

4.3 Heat baths

For the heat baths experiments, the dephasing dependence of the heat flow was measured. The thermal bath that was sent into the AWG had an amplitude of 50 mV corresponding to about 0.3 thermal photons at ω_a while the amplitude of the thermal bath in the SWG was set to zero (around zero thermal photons). In Figure 4.7 the results of this measurement is shown with four different dephasing rates corresponding to the applied noise amplitude being swept from 0-200 mV. Without any dephasing it is evident that no heat flow occurs since no dip or peak can be observed. Once the dephasing rate increases however, a dip in the photon number from the ASWG can be seen accompanied by an increase in photons in the SWG. Thus a net flow of photons from the ASWG to the SWG can be observed. A naive way of determine the temperatures of the respective heat baths would at this point be to extract the temperature using Bose-Einstein statistics (equation 1.2) giving an estimate of the temperatures as $T_a \approx 0.16$ K and T_s close to zero. This entails that the temperature inside of the AWG is higher then in the SWG and that the device in this configuration therefore acts as a heat valve (transporting heat from hot to cold). However, it is important to note that since the Bose-Einstein statistics describes the mean photon number from black-body radiation, one cannot in this case just convert between the photon number and a corresponding temperature. If the thermal bath would instead have a spectral profile corresponding to that of a black body one could relate the measured mean photon number to temperature using Bose-Einstein statistics. For future studies it would also be of interest to actively measure the temperature with the method presented by Marco et.al. [51]. Because we did not send in any heat bath into the SWG it is however reasonable to assume that the temperature inside of the ASWG is higher and thus that the device operates as a heat valve.

The same type of measurement was later performed but with the two mode frequencies tuned away (using a different fluxes) resulting in spectras without dips or peaks. These could be used as base-bands and by subtracting them from the heat flow data the photon flux Φ going into the SWG and ASWG could be estimated by fitting a Gaussian function to the measured data and integrating it. The result is shown in Figure 4.8 and corresponds to the case of $\Gamma_\phi = 0.67$ MHz in Figure 4.7. At this dephasing rate, the photon fluxes were found to be equal $\Phi_s = 0.3 \pm 0.01$ MHz and $\Phi_a = -0.3 \pm 0.02$ MHz indicating that the ASM and SM absorbs and emits an equal number of photons into their respective waveguides. The estimated error bars of these values were found using the covariance matrix of the variable parameters (amplitude, standard deviation and center of the Gaussian) obtained from the fit and propagating their standard deviations to the integral of the Gaussian function. By multiplying the photon fluxes with their respective energies $\hbar\omega_a$ and $\hbar\omega_s$ the actual heat current could be determined as $J_a = -1.05 \pm 0.07$ aW and $J_s = 1.24 \pm 0.05$ aW. Substituting in the values for the experimentally obtained coupling rates into the theoretical expression for the heat flows described by equation 2.64, one also obtains the theoretical values for the heat flows as $J_{a,\text{theory}} = -1.11$ aW and $J_{s,\text{theory}} = 1.22$ aW. The theoretical prediction therefore coincides quite well with the experimentally measured heat flows.

In addition to the dephasing dependence of the heat flow, the amplitude dependence

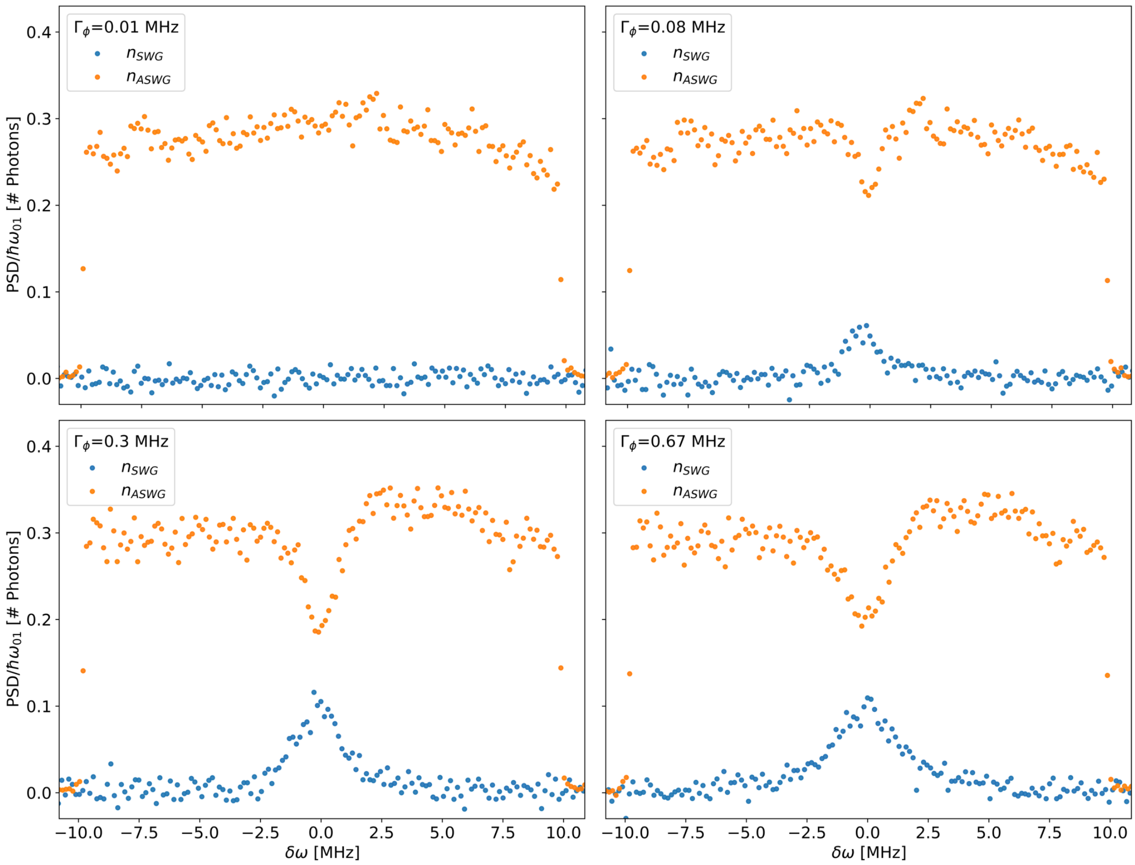

Figure 4.7: PSD measurement of the heat baths sent into the ASWG and SWG for different applied noise amplitudes resulting in different dephasing rates Γ_ϕ. At the lowest dephasing rate no heat flow is observed but at an increasing dephasing rate the photon number decreases in the ASWG and increases in the SWG. A net flow of photons from the ASWG to the SWG is thus observed and due to the high photon number in the ASWG, this configuration therefore corresponds to a heat valve.

of the heat bath sent into the SWG was also investigated at the fixed dephasing rate of $\Gamma_\phi = 0.3$. This was done in order to find the regime where the device operated as a refrigerator, that is the heat flowed from the cold to the hot bath. The condition for this is that $n_a < n_s$ and using Bose-Einstein statistics one finds that this results in that we must have

$$\frac{\omega_a}{\omega_s} < \frac{T_a}{T_s} < 1 \tag{4.1}$$

in order for the device to operate as a refrigerator. However, since $\frac{\omega_a}{\omega_s} \approx 0.92$, for our device, the regime where the device operates as a refrigerator is quite small. By sweeping the amplitude of the heat bath going into the SWG this regime was sought after but not found. The feasibility of finding the refrigeration regime can be theoretically investigated using equation 2.64 in conjunction with Bose-Einstein statistics for the occupation numbers. Keeping to the above mentioned inequality

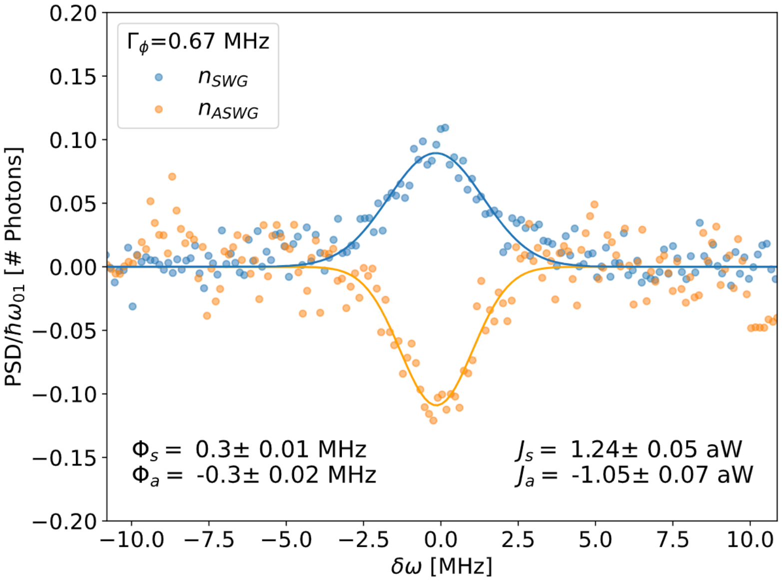

Figure 4.8: Heat currents from ASWG and SWG after subtracting their basebands. By fitting a Gaussian function (variable parameters were amplitude, standard deviation and center), an estimate of the actual heat flows could be made by integrating the obtained function and multiplying with the corresponding photon energies. The photon fluxes Φ are equal (but with opposite sign) and the Heat currents J correspond quite well with theory.

criteria the maximum heat flow as a function of dephasing is found close to where $\frac{T_a}{T_s} = 1$ and converges towards approximately 0.17 aW at high dephasing rates. At the dephasing rate of 0.67 MHz which was the highest dephasing rate investigated in this thesis, the theoretical heat flows in the refrigeration regime were however only found to be 0.08 aW. This is on the same order as the estimated error of the heat flows presented in Figure 4.8 and would therefore be very hard to distinguish. A large increase in the number of averages in addition with higher dephasing rates would therefore have been needed in order to observe refrigeration. In order to reduce the measurement time while increasing the number of averages, purely FPGA based measurements where both the PSD calculations and the interleaved averaging is taking place on hardware would be desirable for future experiments on this device. However, with increasing dephasing rates, a broadening of the dips and peaks were observed. The reason of this is unclear but it results in that observed heat flows would become harder to distinguish if one only used the dephasing as a way of increasing the refrigeration. Another way of improving the chances to observe refrigeration is to increase the radiative coupling rates to the waveguides with a redesigned device.

5

Conclusion

This study began by tuning the two qubits into a fully hybridized state and mapping applied flux-line voltages to magnetic flux. The coupling rates were then determined through spectroscopy and by applying noise through one of the flux lines with a centre frequency of $2g$, a linear relationship between the pure dephasing rate and the applied noise power was found. Using Mollow triplets the PSD measurements could be calibrated to reflect the number of photons present in the two waveguides. This calibration also gave an indication to the noise photons added by the amplification chain in each output line which for the one including the TWPA was about 3.5 times less than the line without a TWPA. The TWPA therefore resulted in a much improved SNR meaning that fewer averages were needed and since both the interleaved averaging and the PSD calculations were done in software, the TWPA could greatly reduce the measurement time. In fact, it was the measurement time that was a limiting factor in this project, making large sweeps over many different parameters (such as many different dephasing rates) infeasible. It would therefore be desirable in future experiments to have a TWPA in both output lines in addition to performing the PSD and averaging on a FPGA which would allow for more averages with better SNR taken over a shorter time.

The center peak of the Mollow triplet was also used for clear observations of excitation transfer as a consequence of dephasing. With increased dephasing, the photon flux into the SWG was observed to decrease while the flux into the ASWG increased. The same concept of excitation transfer induced by dephasing was later used to measure heat flow where we present the workings of a heat valve. The maximum heat flows observed corresponded well with the theoretical model and occurred at the largest dephasing rate that was investigated. The conclusion could therefore be made that in this configuration of the device, it operated as a heat valve which drove the heat current from the hot ASWG to the cold SWG. Because the largest heat flow was observed for the largest dephasing rate that was investigated, it would also be of interest to explore the heat valve at higher dephasing regimes.

In summary, this project has shown how to operate a novel quantum thermal machine as a heat valve on a cQED platform. In state of the art measurements, synthesised thermal fields were used to control the temperature of two waveguides. Through noise induced excitation transfers caused by dephasing we could then observe heat flows on the aW scale between the waveguides, that coincided well with the theoretical predictions. Hopefully these results help to solidify cQED as a robust platform for performing experiments in quantum thermodynamics and also to pave the way towards one day finding a quantum advantage in thermodynamics.

Bibliography

[1] J. P. Dowling, G. J Milburn. Quantum technology: the second quantum revolution. The royal society publishing, 15 August 2003, 361:1809.

[2] M. Brune, E. Hagley, J. Dreyer, X. Maître, A. Maali, C. Wunderlich, J. M. Raimond, and S. Haroche, “Observing the Progressive Decoherence of the “Meter” in a Quantum Measurement”, Phys. Rev. Lett. 77, 4887–4890 (1996).

[3] C. Monroe, D. M. Meekhof, B. E. King, and D. J. Wineland, “A “Schrödinger Cat” Superposition State of an Atom”, Science 272, 1131–1136 (1996).

[4] “Measuring and Manipulating individual Quantum Systems”, The Royal Swedish Academy of Science (2012).

[5] R. P. Feynman, “Simulating physics with computers”, International Journal of Theoretical Physics 21, 467–488 (1982).

[6] M. A. Nielsen and I. L. Chuang, Quantum Computation and Quantum Information (Cambridge University Press, 2000).

[7] Arute, F., Arya, K., Babbush, R. et al. Quantum supremacy using a programmable superconducting processor. Nature 574, 505–510 (2019).

[8] E. Pednault, J Gunnels, D. Maslov, and J. Gambetta, “On Quantum Supremacy””, IBM Research Blog (2019).

[9] Charge-insensitive qubit design derived from the Cooper pair box Jens Koch, Terri M. Yu, Jay Gambetta, A. A. Houck, D. I. Schuster, J. Majer, Alexandre Blais, M. H. Devoret, S. M. Girvin, and R. J. Schoelkopf Phys. Rev. A 76, 042319 – Published 12 October 2007.

[10] Aaron Kraft, Christoph Rupprecht, Yau-Chuen Yam, Superconducting Quantum Interference Device (SQUID), UBC PHYSICS 502 PROJECT (2017 FALL).

[11] G Wendin, “Quantum information processing with superconducting circuits: a review”, Reports on Progress in Physics 80, 106001 (2017).

[12] Emely Wiegand (2021), Quantum Optics and Waveguide Quantum Electrodynamics in Superconducting Circuits, Chalmers University of Technology.

[13] T. Tufarelli, F. Ciccarello, and M. S. Kim, “Dynamics of spontaneous emission in a single-end photonic waveguide”, Phys. Rev. A 87, 013820 (2013).

[14] Mukherjee, V., Kofman, A.G. & Kurizki, G. Anti-Zeno quantum advantage in fast-driven heat machines. Commun Phys 3, 8 (2020).

[15] B. Bhandari et al., “Geometric properties of adiabatic quantum thermal machines,” Phys. Rev. B 102, 155407 (2020).

[16] G. Benenti, G. Casati, K. Saito, and R. S. Whitney, “Fundamental aspects of steady-state conversion of heat to work at the nanoscale,” Physics Reports 694, 1 – 124 (2017).

[17] R. P. Feynman. Lectures on physics, volume vol I. Pearson Addison-Wesley, 2006.

[18] P. Rebentrost, M. Mohseni, I. Kassal, S. Lloyd, and A. Aspuru-Guzik, “Environment-assisted quantum transport,” New Journal of Physics, vol. 11, p. 033003, Mar. 2009.

[19] Arno Bargerbos, Analog Quantum Simulation of Noise Assisted Transport in Light Harvesting Structures with Superconducting Circuits, ETH, October 6th, 2016.

[20] M. O. Scully and M. S. Zubairy, Quantum Optics. Cambridge University Press, 1997.

[21] K. H. Onnes. The Superconductivity of Mercury. Comm. Phys. Lab. Univ. Leiden, 122:251, 1911.

[22] R. P. Feynman. Lectures on physics, volume vol III. Pearson Addison-Wesley, 2006.

[23] Nave, Carl R. (2006). "The BCS Theory of Superconductivity". Hyperphysics. Dept. of Physics and Astronomy, Georgia State Univ.

[24] M. H. Devoret, in Quantum Fluctuations (Les Houches Session LXIII), edited by S. Reynaud, E. Giacobino, and J. Zinn- Justin (Elsevier, New York, 1997), pp. 351–386.

[25] B. D. Josephson, “Possible new effects in superconductive tunnelling,” Physics Letters, vol. 1, pp. 251–253, July.

[26] Alexandre Blais, Arne L. Grimsmo, S. M. Girvin, Andreas Wallraff, "Circuit quantum electrodynamics", Reviews of modern physics, VOLUME 93, APRIL–JUNE 2021.

[27] S. Berger, Geometric phases and noise in circuit QED. PhD thesis, ETH Zurich, 2015.

[28] J. Koch, T. M. Yu, J. Gambetta, A. A. Houck, D. I. Schuster, J. Majer, A. Blais, M. H. Devoret, S. M. Girvin, and R. J. Schoelkopf, “Chargeinsensitive qubit design derived from the Cooper pair box,” Phys. Rev. A, vol. 76, no. 4, p. 042319, 2007.

[29] V. Bouchiat, D. Vion, P. Joyez, D. Esteve, and M. H. Devoret, “Quantum coherence with a single Cooper pair,” Phys. Scr., vol. T76, pp. 165–170, 1998.

[30] L. S. Bishop, Circuit Quantum Electrodynamics. Michigan: Proquest, 1st ed ed., 2011.

[31] D. M. Pozar, Microwave Engineering (Wiley, 2005)

[32] K. Lalumi‘ere, B. C. Sanders, A. F. van Loo, A. Fedorov, A. Wallraff, and A. Blais, “Input-output theory for waveguide qed with an ensemble of inhomogeneous atoms,” Phys. Rev. A, vol. 88, p. 043806, Oct 2013.

[33] G.Wendin, "Quantum Information Processing with Superconducting Circuits: a Review" arXiv:1610.02208v2 [quant-ph] 8 Oct 2017.

[34] J.J. Sakurai, Jim Napolitano, "Modern Quantum Mechanics" Second edition, Camebridge University Press 2017.

[35] H.-P. Breuer and F. Petruccione. "The theory of open quantum systems". Oxford University Press, 2006.

[36] C. W. Gardiner and P. Zoller. Quantum Noise. Springer, 2004

[37] S. R. Sathyamoorthy, “Quantum Optics in Superconducting Circuits”, PhD thesis (Department of Microtechnology and Nanoscience, 2017).

[38] M. K. Tey, Z. Chen, S. A. Aljunid, B. Chng, F. Huber, G. Maslennikov, and C. Kurtsiefer, “Strong interaction between light and a single trapped atom without the need for a cavity,” Nat. Phys., vol. advanced online publication, pp. –, Oct. 2008.

[39] K. Lalumi‘ere, B. C. Sanders, A. F. van Loo, A. Fedorov, A. Wallraff, and A. Blais, “Input-output theory for waveguide qed with an ensemble of inhomogeneous atoms,” Phys. Rev. A, vol. 88, p. 043806, Oct 2013.

[40] K. Lalumiere, B. C. Sanders, A. F. van Loo, A. Fedorov, A. Wallraff, and ‘ A. Blais. Input-output theory for waveguide qed with an ensemble of inhomogeneous atoms. Phys. Rev. A, 88:043806, Oct 2013.

[41] Lu, Y., Bengtsson, A., Burnett, J.J. et al. Characterizing decoherence rates of a superconducting qubit by direct microwave scattering. npj Quantum Inf 7, 35 (2021).

[42] B. K. Mitchell, “Nonclassical light in waveguide qed: Amplitude and intensity correlations,” Master’s thesis, ETH Zurich, 2016.

[43] M. Mitchison, “Pure dephasing gf in a master equation and noise power spectral densities.”, `http://physics.stackexchange.com/q/282909.`

[44] M. H. Devoret, “Quantum fluctuations in electrical circuits,” in Quantum Fluctuations: Les Houches Session LXIII (S. Reynaud, E. Giacobino, and J. Zinn-Justin, eds.), pp. 351–386, Elsevier, 1997.

[45] A. Asadian, D. Manzano, M. Tiersch, and H. J. Briegel, "Heat transport through lattices of quantum harmonic oscillators in arbitrary dimensions", PHYSICAL REVIEW E 87, 012109 (2013).

[46] BlueFors LD Dilution Refrigerator System `https://bluefors.com/products/ld-dilution-refrigerator/`

[47] Kowshik Erappaji Patel, "Engineering decay rates of Hybridised modes in Superconducting circuits", Master thesis Chalmers, 2020.

[47] Baleegh Abdo, "Rising above the noise: quantum-limited amplifiers empower the readout of IBM Quantum systems", IBM research blog, January 29, 2020.

[48] Arpit Ranadive, Martina Esposito, Luca Planat, Edgar Bonet, C ́ecile Naud, Olivier Buisson, Wiebke Guichard, and Nicolas Roch, "A reversed Kerr traveling wave parametric amplifier", arXiv:2101.05815v2 [quant-ph], February 8, 2021.

[49] J. Fink, Quantum nonlinearities in strong coupling circuit QED. PhD thesis, ETH Zurich, 10 2010.

[50] Slawomir Simbierowicz, Visa Vesterinen, Joshua Milem, Aleksi Lintunen, Mika Oksanen, Leif Roschier, Leif Grönberg, Juha Hassel, David Gunnarsson, and Russell E. Lake, "Characterizing cryogenic amplifiers with a matched temperature-variable noise source", arXiv:2009.03010v2 [quant-ph] Feb 25, 2021.

[51] Marco Scigliuzzo, Andreas Bengtsson, Jean-Claude Besse, Andreas Wallraff, Per Delsing, and Simone Gasparinetti, "Primary Thermometry of Propagating Microwaves in the Quantum Regime", Phys. Rev. X 10, 041054 – Published 17 December 2020.

[52] Vinjanampathy and Anders, Quantum Thermodynamics, Contemporary Physics 57, 545 (2016).

[53] R. Uzdin et. al, Equivalence of Quantum Heat Machines, and Quantum-Thermodynamic Signatures, Phys. Rev. X 5, 031044 (2015).

[54] M. Lostaglio, Certifying Quantum Signatures in Thermodynamics and Metrology via Contextuality of Quantum Linear Response, Phys. Rev. Lett. 125, 230603 (2020).

[55] L. Bresque, P. A. Camati, S. Rogers, K. Murch, A. N. Jordan, and A. Auffèves, Two-Qubit Engine Fueled by Entanglement and Local Measurements, Phys. Rev. Lett. 126, 120605 (2021).

[56] L. Buffoni et. al, Quantum Measurement Cooling, Phys. Rev. Lett. 122, 070603 (2019).

[57] Yong Lu et.al “Nonequilibrium heat transport and work with a single articial atom coupled to a waveguide: emission without external driving”, arXiv: 27 Jul 2021.

[58] Bivas Dutta. "Energetics in metallic-island and quantum-dot based single-electron device". Condensed Matter [cond-mat]. Université Grenoble Alpes, 2018.

[59] James Klatzow et.al. "Experimental Demonstration of Quantum Effects in the Operation of Microscopic Heat Engines", Phys. Rev. Lett. 122, 110601 – Published 20 March 2019.

[60] Arjan F. van Loo et. al, "Photon-mediated interactions between distant artificial atoms", arXiv:1407.6747, 24 Jul 2014.

[61] O.Astafiev et.al. "Resonance Fluorescence of a Single Artificial Atom", Science, Vol 327, Issue 5967, pp. 840-843, 12 Feb 2010.

[62] J. Fourier, Théorie Analytique de la Chaleur, Didot, Paris (1822).

[63] J. J. Burnett, A. Bengtsson, M. Scigliuzzo, D. Niepce, M. Kudra, P. Delsing, and J. Bylander, "Decoherence Benchmarking of Superconducting Qubits", Npj Quantum Information, 5, 1 (2019).

[64] C. MACKLIN et.al., "A near–quantum-limited Josephson traveling-wave parametric amplifier", Science, Vol 350, Issue 6258, pp. 307-310, 3 Sep 2015.

DEPARTMENT OF SOME SUBJECT OR TECHNOLOGY
CHALMERS UNIVERSITY OF TECHNOLOGY
Gothenburg, Sweden
www.chalmers.se